AGU PUBLICATIONS

Tectonics

RESEARCH ARTICLE
10.1002/2015TC003920

Key Points:
- New P-T-time data from high-pressure rocks, southern New England Orogen
- High-pressure rocks record evidence of Early Ordovician subduction rollback
- Tasmanides formed above a long-lived retreating subduction zone

Correspondence to:
G. Phillips,
glen.phillips@industry.nsw.gov.au

Citation:
Phillips, G., R. Offler, D. Rubatto, and D. Phillips (2015), High-pressure metamorphism in the southern New England Orogen: Implications for long-lived accretionary orogenesis in eastern Australia, *Tectonics*, *34*, 1979–2010, doi:10.1002/2015TC003920.

Received 7 MAY 2015
Accepted 26 AUG 2015
Accepted article online 1 SEP 2015
Published online 30 SEP 2015
Corrected 12 NOV 2015

This article was corrected on 12 NOV 2015. See the end of the full text for details.

High-pressure metamorphism in the southern New England Orogen: Implications for long-lived accretionary orogenesis in eastern Australia

G. Phillips[1,2], R. Offler[3], D. Rubatto[4], and D. Phillips[5]

[1]Division of Resources and Energy, Department of Industry, Geological Survey of NSW, Maitland, NSW, Australia, [2]Discipline of Earth Sciences, School of Environmental and Life Sciences, University of Newcastle, Callaghan, NSW, Australia, [3]New South Wales Institute of Frontiers Geoscience, School of Environmental and Life Sciences, University of Newcastle, Newcastle, NSW, Australia, [4]Research School of Earth Sciences, Australian National University, Canberra, ACT, Australia, [5]School of Earth Sciences, University of Melbourne, Parkville, Vic, Australia

Abstract New geochemical, metamorphic, and isotopic data are presented from high-pressure metamorphic rocks in the southern New England Orogen (eastern Australia). Conventional and optimal thermobarometry are augmented by U-Pb zircon and $^{40}Ar/^{39}Ar$ phengite dating to define pressure-temperature-time (*P-T-t*) histories for the rocks. The *P-T-t* histories are compared with competing geodynamic models for the Tasmanides, which can be summarized as (i) a retreating orogen model, the Tasmanides formed above a continuous, west dipping, and eastward retreating subduction zone, and (ii) a punctuated orogen model, the Tasmanides formed by several arc accretion, subduction flip, and/or transference events. Whereas both scenarios are potentially supported by the new data, an overlap between the timing of metamorphic recrystallization and key stages of Tasmanides evolution favors a relationship between a single, long-lived subduction zone and the formation, exhumation, and exposure of the high-pressure rocks. By comparison with the retreating orogen model, the following links with the *P-T-t* histories emerge: (i) exhumation and underplating of oceanic eclogite during the Delamerian Orogeny, (ii) recrystallization of underplated and exhuming high-pressure rocks at amphibolite facies conditions coeval with a period of rollback, and (iii) selective recrystallization of high-pressure rocks at blueschist facies conditions, reflecting metamorphism in a cooled subduction zone. The retreating orogen model can also account for the anomalous location of the Cambrian-Ordovician high-pressure rocks in the Devonian-Carboniferous New England Orogen, where sequential rollback cycles detached and translated parts of the leading edge of the overriding plate to the next, younger orogenic cycle.

1. Introduction

The southern Tasmanides of eastern Australia record a 320 million year history (520–200 Ma) of active margin tectonism and prolific continental growth [*Glen*, 2005; *Kemp et al.*, 2009]. The evolution of the southern Tasmanides is divided into three main orogenic stages, which represent key periods of development [*Glen*, 2005]. From west to east, these stages are the (i) Delamerian Orogeny, (ii) Lachlan Orogeny, and (iii) New England Orogeny (Figure 1a). Whereas the influence of subduction is widely acknowledged as the driver of orogenesis during each stage, the number and polarity of subduction zones, along with the mechanism(s) responsible for the transition from one stage to the next, remain widely contested [*Crawford and Berry*, 1992; *Collins*, 2002; *Fergusson*, 2003; *Gray and Foster*, 2004; *Glen*, 2005; *Foden et al.*, 2006; *Offler and Murray*, 2011; *Cayley*, 2011; *Aitchison and Buckman*, 2012]. Central to the debate is whether the Tasmanides formed as a retreating orogen above a continuous subduction zone [*Collins*, 2002] or by punctuated collision and accretion events that resulted in polarity reversals or transference to a new or existing subduction zone [*Aitchison and Buckman*, 2012]. In the retreating orogen model, the Tasmanides formed in a suprasubduction setting with tectonism driven by a dominant, west dipping, eastward retreating subduction zone [*Collins*, 2002]. This model relies on periods of rollback to explain the outward retreat of the subduction zone, which in turn results in the initiation of the next, younger orogenic stage. Based on this model, continental growth largely manifests in the back-arc region of the orogen through basin development, extensive sediment deposition, and juvenile magmatism [*Foster and Gray*, 2000; *Collins*, 2002; *Kemp et al.*, 2009]. In contrast, the punctuated collision and accretion model involves collisions, terrane accretions, and subduction transference to explain the outward growth of the orogen [*Aitchison and Buckman*, 2012]. In this case, continental growth

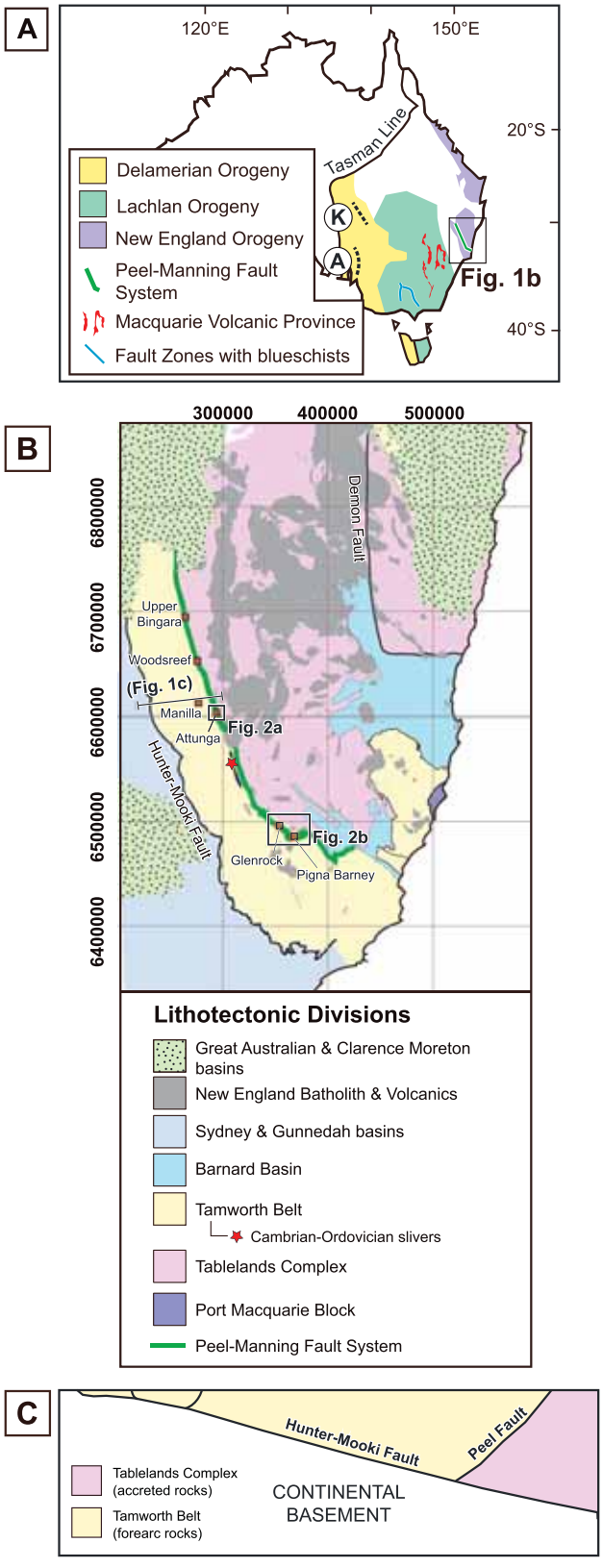

is facilitated by the frontal accretion of magmatic arcs or outboard terranes in the fore-arc region of the orogen. The subsequent blocking of the subduction zone can result in a flip of subduction polarity or outboard transference to an existing subduction zone [*Stern*, 2004].

To explore the applicability of the two geodynamic models, we examine blocks of high-pressure metamorphic rocks that are situated in serpentinite matrix mélange shear zones in the southern New England Orogen (Figures 1a and 1b). Ambiguity surrounds the relevance of these rocks, as sparse U-Pb [*Aitchison et al.*, 1992; *Aitchison and Ireland*, 1995; *Fanning et al.*, 2002] and potentially imprecise K-Ar [*Fukui et al.*, 1995] age data yield Cambrian and Ordovician ages, which are at least 100 million years older than the timing of continent margin subduction (360–300 Ma) [*Leitch*, 1974]. If these data accurately constrain the timing of subduction zone metamorphism, the pressure-temperature-time (*P-T-t*) histories recorded by these rocks have the potential to provide insight into an early and poorly understood stage of the New England Orogen. To test the competing models, we compare these

Figure 1. Locality maps of regional geology and the study locale. (a) Simplified map of eastern Australia showing the main orogenic stages that define the development of the Tasmanides. Dashed lines represent the main sectors of the Delamerian Orogen. Abbreviations: A = Adelaidean Belt; K = Koonenberry Belt. (b) Enlarged map of the southern New England Orogen showing the distribution of the main tectonostratigraphic units. The high-pressure metamorphic rocks were collected from the Peel-Manning Fault System at Attunga, Glenrock, and Pigna Barney. The locations of enlarged maps shown in Figures 2a (Attunga) and 2b (Glenrock and Pigna Barney) are provided. Note the location of the seismic line from which the cross section shown in Figure 1c was constructed. (c) Cross section through the Manilla region showing the fore-arc accretionary wedge architecture. The cross section was constructed from depth-converted seismic data, mapped geology, and the interpretation of *Korsch et al.* [1997].

P-T-t histories with coeval stages of Tasmanides development. For continuous subduction, high-pressure rocks should record metamorphic ages that span the longevity of the Tasmanides and *P-T* histories that reflect important evolutionary stages of the Delamerian and Lachlan orogens. In the case of punctuated subduction, subduction complexes should get progressively younger across the Tasmanides (from west to east) and be located inboard of accreted intraoceanic arcs. Following arc-continent collision, flip or outboard transference of subduction results in the isolation of an obducted subduction complex from the new active margin. This model therefore predicts the high-pressure rocks in the New England Orogen to have formed in a subduction zone that was unrelated to the development of the Delamerian and Lachlan orogens.

In this paper, we present new metamorphic, geochemical, and geochronological data from high-pressure metamorphic rocks in the Peel-Manning Fault System. To date, these rocks have received limited attention, with few attempts made to quantify the conditions of metamorphism or to determine *P-T-t* histories [*Shaw and Flood*, 1974; *Offler*, 1999]. Linking of the metamorphic and temporal records is also yet to be attempted, resulting in uncertainty in the available U-Pb age data (i.e., protolith crystallization or metamorphism). The timing of exhumation, as recorded by rocks metamorphosed at blueschist facies conditions, is also unclear due to the widespread application of whole-rock K-Ar dating and the potential problems associated with excess argon [*Fukui et al*., 1995; *Arnaud and Kelley*, 1995]. This ambiguity makes it difficult to reconcile the evolution of high-pressure metamorphic rocks with geodynamic models of the New England Orogen and greater Tasmanides. To overcome these problems, we present new data from four high-pressure metamorphic rocks, which specifically includes (i) whole-rock trace element composition to determine the protolith of the high-pressure metamorphic rocks, which has bearing on exhumation mechanics, (ii) detailed petrology to identify mineral reaction textures and to determine the relative timing of metamorphic mineral growth, (iii) mineral compositional data to identify compositional zoning in the minerals and to obtain pressure and temperature conditions of metamorphism by conventional and optimal thermobarometry, (iv) U-Pb isotopic and trace element geochemistry of zircons from eclogite to ascertain the timing of metamorphism, and (v) $^{40}Ar/^{39}Ar$ dating of phengite from blueschists to determine the timing of exhumation. Using these data, we attempt to reconcile the formation of the high-pressure metamorphic rocks and the encompassing serpentinite matrix mélange with geodynamic models of the Tasmanides.

2. Background Geology

2.1. The Tasmanides

The southern Tasmanides formed during three main orogenic stages, which from west to east (present-day coordinates) are (i) the Delamerian Orogen, (ii) the Lachlan Orogen, and (iii) the New England Orogen [*Glen*, 2005] (Figure 1a). The Delamerian Orogeny affected the Neoproterozoic passive margin of eastern Australia from early Cambrian to early Ordovician times (520–490 Ma) [*Foden et al*., 2006; *Greenfield et al*., 2011]. A Gondwana-wide synthesis of the Delamerian Orogen is provided by *Cawood* [2005], with critical information concerning the evolution of the Australian mainland presented herein. The effects of the Delamerian Orogeny are well preserved in the Koonenberry and Adelaidean belts (Figure 1a), where Cambrian-aged igneous rocks of calc-alkaline, tholeiitic, and boninitic affinity are interpreted to represent parts of an active margin [*Crawford et al*., 1984; *Foden et al*., 2006; *Greenfield et al*., 2011; *Glen*, 2013]. In the Koonenberry Belt, *Greenfield et al*. [2011] suggest that the eastern margin of Australia was in an Andean-type setting during middle to late Cambrian times, a view that is challenged by the work of *Crawford et al*. [1997], who suggest that calc-alkaline rocks in the Koonenberry Belt formed in an immature continental rift setting. *Glen* [2013] expands on the Andean-type model of *Greenfield et al*. [2011] to provide a mechanism that also explains the presence of Cambrian-aged rocks in the Peel-Manning Fault System. Given that these rocks are slightly older (>530 Ma) and located ~1000 km to the east of the Koonenberry Belt, *Glen* [2013] suggests that two subduction zones were active during the Early to Middle Cambrian: the first active between 530 and 520 Ma in an intraoceanic setting located outboard of the continental margin and a second, west dipping subduction zone active between 520 and 500 Ma below the continental margin. The main implication of this model is that it requires the rocks located in the Peel-Manning Fault System to have formed in a subduction zone that was unrelated to the main west dipping subduction zone responsible for the Delamerian orogenic stage of the Tasmanides. The timing of convergent deformation related to the Delamerian Orogeny is defined by isotopic dating of magmatic units that show prekinematic to postkinematic relationships with the regional finite strain pattern [*Foden et al*., 2006; *Greenfield et al*., 2011]. In the Koonenberry Belt,

U-Pb zircon dating of prekinematic and postkinematic dykes restricts the timing of convergence to between 504.5 ± 2.6 Ma and 496 ± 3.1 Ma [*Greenfield et al*., 2011]. In the Adelaidean Fold Belt (Figure 1a), U-Pb isotopic dating of pretectonic and posttectonic magmatic rocks signifies a longer period of convergence between 514 ± 3 Ma and 490 ± 3 Ma [*Foden et al*., 2006]. The cessation of active margin convergence is marked by a regional disconformity in the Koonenberry Belt and the emplacement of postorogenic magmatic rocks in the Adelaidean Belt [*Crawford et al*., 1984; *Foden et al*., 2006; *Greenfield et al*., 2011].

Following the Delamerian Orogeny, evidence of subduction-related magmatism is preserved in the Macquarie Volcanic Province [*Crawford et al*., 2007], which comprises a linear belt of Ordovician-Silurian volcanic rocks that are located approximately 700 km to the east of the Koonenberry Belt (Figure 1a). Where it is yet to be unequivocally shown, there is growing support that the transfer from the Delamerian to Lachlan orogenic stage was caused by rollback of the subduction zone [*Foden et al*., 2006; *Cayley et al*., 2012]. A wealth of information is available for the Lachlan Orogen, and a detailed synthesis of the geology of the orogen is provided by *Gray and Foster* [2004] or *Glen* [2005, 2013]. Herein, we provide a brief discussion of the salient features of the orogen which have led to the publication of numerous conflicting geodynamic models. The orogen contains sparse exposures of Cambrian-aged mafic rocks comprising boninite and low-Ti andesite-tholeiite [*Crawford et al*., 1984], along with voluminous Lower-Middle Ordovician quartz-rich turbidites and lesser Late Ordovician black shales that are intruded/extruded by Silurian-Devonian-aged granites (Figure 1a) [*Fergusson and Coney*, 1992; *Vandenberg*, 1999; *Meffre et al*., 2007; *Kemp et al*., 2009]. Confined to narrow north-south striking belts, the basaltic-andesitic rocks of the Macquarie Volcanic Province are interpreted to represent the remnants of a magmatic arc [*Glen et al*., 1998; *Crawford et al*., 2007] or partially melted parts of enriched upper mantle that were later exposed during back-arc extension [*Quinn et al*., 2014]. Given the predominant distribution of turbidites in the west and the subduction-related volcanic rocks of the Macquarie Volcanic Province in the east, most workers support a model where the Lachlan Orogen formed in a broad back-arc setting behind an east facing magmatic arc (i.e., Japan Sea-type setting) [*Powell*, 1983; *Fergusson and Coney*, 1992; *Glen et al*., 1998; *Collins*, 2002]. However, whether the Macquarie Volcanic Province represents the remnants of that arc remains a topic of considerable debate [*Quinn et al*., 2014; *Fergusson*, 2014]. The identification of major fault zones locally containing blueschists in the turbidite package also led *Gray and Foster* [1997] to expand on the back-arc basin model and suggest a multiple-subduction scenario similar to that of the Philippine Sea. In contrast to the back-arc models, *Aitchison and Buckman* [2012] suggest that the Macquarie Volcanic Province formed as a magmatic arc above an east dipping subduction zone, which was accreted to the eastern margin of Australia in the late Ordovician-early Silurian. This collision resulted in the termination of east dipping subduction and transference to an existing west dipping intraoceanic subduction zone that was located to the east of the collision zone. Irrespective of the contrasting geodynamic settings, emergence of the Lachlan Orogen by the Late Devonian to Carboniferous times is shown by the presence of a thick molasses-like overlap sequence [*Foster and Gray*, 2000]. By this time, subduction-related orogenesis had migrated further to the east, manifesting as the New England Orogeny.

The Southern New England Orogen is made up of five main tectonostratigraphic units: (i) Cambrian-Silurian, tectonized and serpentinized ultramafic to mafic rocks in the Peel-Manning Fault System, (ii) Late Devonian-Carboniferous rocks of the Tamworth Belt, which also contain narrow (<1 km) horizons of Cambrian-Ordovician volcaniclastic sedimentary rocks near the Peel-Manning Fault System [*Leitch and Cawood*, 1987], (iii) Silurian-Carboniferous accretionary complex rocks of the Tablelands Complex, (iv) Permian-Triassic plutonic and volcanic rocks of the New England Batholith, and (v) Early Permian sedimentary rocks of the Barnard Basin (Figure 1b) [*Leitch*, 1974]. Cambrian-Devonian-aged rocks located in the eastern part of the Tamworth Belt (collectively called the Gamilaroi Terrane) [*Aitchison and Flood*, 1994] provide insight into the early history of the orogen. The Cambrian-Ordovician volcaniclastic sequences are interpreted to represent sediments derived from an intraoceanic volcanic arc located to the west, thus placing the New England Orogen in a fore-arc setting at this time [*Cawood*, 1983; *Leitch and Cawood*, 1987]. Devonian-aged volcanic rocks show geochemical signatures that are consistent with derivation in an island arc to proximal back-arc setting [*Aitchison and Flood*, 1994; *Offler and Gamble*, 2002; *Offler and Murray*, 2011], which are interpreted to reflect a variety of different geodynamic scenarios, ranging from (i) a single west dipping subduction zone [*Offler and Gamble*, 2002], (ii) a single east dipping subduction zone followed by arc accretion and subduction flip [*Aitchison and Flood*, 1994], and (iii) simultaneous east and west dipping subduction zones [*Offler and Murray*, 2011]. Whereas the number and polarity of subduction zone(s) during the Late Silurian-Devonian evolution of the southern New England

Orogen are unresolved, the facing of fore-arc and accretionary components supports an east facing Andean-type setting for the orogen throughout the Carboniferous [*Leitch*, 1974]. In situ evidence of continental arc magmatism associated with west dipping subduction is rare [*Wilkinson*, 1971], but extensive horizons of calc-alkaline ignimbrites recording Carboniferous U-Pb zircon ages are interlayered with volcaniclastic- and lithic-rich sandstones of the Tamworth Belt [*McPhie*, 1984, 1987; *Roberts et al*., 2003, 2004, 2006]. To the east of the Tamworth Belt, progressive accretion of lower plate sequences has resulted in a general west to east younging of rocks in the Tablelands Complex [*Aitchison et al*., 1988; *Ishiga et al*., 1988]. Rocks of the Permian-Triassic New England Batholith dominantly intrude the Tablelands Complex and comprise a chemically and isotopically diverse suite of felsic plutonic and volcanic rocks (Figure 1b) [*Shaw and Flood*, 1981; *Hensel et al*., 1985; *Kemp et al*., 2009; *Phillips et al*., 2011]. The emplacement of these magmatic rocks from the Early Permian is interpreted to represent a switch in thermal gradient, which coincided with a change from accretionary to back-arc [*Dirks et al*., 1992; *Jenkins et al*., 2002; *Phillips et al*., 2008] or transform margin setting [*Aitchison and Flood*, 1992]. The deposition of deep-shallow marine sediments comprising the Barnard Basin [*Leitch*, 1988] occurred coevally with the incipient stages of Batholith emplacement, which was probably related to crustal extension associated with the change in geodynamic setting [*Jenkins et al*., 2002]. The late-stage emplacement of plutonic rocks with geochemical and isotopic signatures consistent with postorogenic magmas signifies the cratonization of the New England Orogen by the late Triassic [*Phillips et al*., 2011].

2.2. The Peel-Manning Fault System

The Peel-Manning Fault System in the Southern New England Orogen is a tectonic boundary between the Tamworth Belt and Tablelands Complex (Figure 1b). The fault system is curvilinear, striking in a north-south orientation in the north and a northwest-southeast orientation in the south (Figure 1b). Seismic imaging across the fault system at Manilla (Figure 1b) reveals a general west dipping structure that is truncated by an east dipping décollement surface that separates rocks of the fore-arc basin from the continental basement (Hunter-Mooki Fault; Figure 1c). The Peel-Manning Fault System is characterized by fault-bounded sequences of serpentinite matrix mélange, norite, gabbro, pyroxenite, dolerite, basalt, plagiogranite, and chert [*Cross*, 1983; *Blake and Murchey*, 1988; *Aitchison et al*., 1994]. Relict blocks of harzburgite, along with exotic blocks of eclogite, blueschist, amphibolite, plagiogranite, basalt, and chert are located in the serpentinite matrix mélange; which is interpreted to represent a heavily tectonized harzburgite layer of the original ophiolite sequence [*Cross*, 1983; *Blake and Murchey*, 1988; *Aitchison et al*., 1994; *O'Hanley and Offler*, 1992; *Offler*, 1999]. Even though fault bounded, the sequence of rocks in the Peel-Manning Fault System is interpreted to represent a dismembered and attenuated ophiolite (termed the Peel-Manning Ophiolite herein) [*Cross*, 1983; *O'Hanley and Offler*, 1992; *Yang and Seccombe*, 1997; *Aitchison et al*., 1994]. Where a coherent stratigraphic section is yet to be identified, facing of the fault-bounded sequences indicates that the ophiolite probably faces to the west [*Cross*, 1983; *Aitchison et al*., 1994; *Yang and Seccombe*, 1997].

Geochemical analysis of relict chromite in harzburgite and immobile trace elements in dolerite from the Upper Bingara region (Figure 1b) indicates that the ultramafic to intermediate rocks of the ophiolite formed in a back-arc setting [*Yang and Seccombe*, 1997]. In the south at Pigna Barney (Figure 1b), whole-rock analyses of basaltic rocks have a low-Ti signature that is consistent with crystallization from a more refractory melt generated from a depleted source [*Cross*, 1983]. Given that these basalts are interlayered with boninites, *Cross* [1983] interpreted the sequence to have formed in an island arc to fore-arc setting. Most of the exotic blocks in the serpentinite matrix mélange layer preserve the effects of low-grade metamorphism (prehnite-pumpellyite facies), which has partially recrystallized the original igneous textures and mineral assemblages [*Offler*, 1982; *Cross*, 1983; *Sano et al*., 2004; *Offler and Shaw*, 2006]. Oxygen isotope thermometry on serpentine-magnetite mineral pairs from samples at Woodsreef (Figure 1b) reveals temperature in the range of 350 to 220°C for the serpentinization of the harzburgite [*O'Hanley and Offler*, 1992].

Temporal constraints on the formation of the ophiolite are provided by isotopic dating of exotic blocks contained in the serpentinite matrix mélange. Blocks of plagiogranite located at Upper Bingara, Woodsreef, and Manilla yield U-Pb zircon ages of ca. 530 Ma [*Aitchison et al*., 1992; *Aitchison and Ireland*, 1995]. The blocks are interpreted to represent late-stage differentiates of basic magmas and, therefore, provide a crystallization age for the ophiolite [*Aitchison et al*., 1992; *Aitchison and Ireland*, 1995]. In the southern part of the fault system at Glenrock (Figure 1b), Sm-Nd dating of a block of metadiorite yielded an age of 536 ± 38 Ma [*Sano et al*., 2004]. This age is interpreted to represent the timing of protolith crystallization. Isotopic dating of rocks recording the

Table 1. Summary Table of Sample Locations and Calculated U-Pb or $^{40}Ar/^{39}Ar$ Isotopic Ages

		Coordinates			$^{40}Ar/^{39}Ar$ Age	
Sample	Locality	Latitude	Longitude	U-Pb Age	Step Heating	Laser
AT2	Attunga	30°50′39.7″	150°54′45.2″	514 ± 6 Ma	na	na
				480 ± 5 Ma	na	na
7936	Glenrock	31°43′05.7″	151°28′29.6″	na	479 ± 1 Ma	482 ± 1 Ma
47302	Pigna Barney	31°47′26.1″	151°34′52.1″	na	na	na
PB3C	Pigna Barney	31°47′25.2″	151°36′52.1″	na	478 ± 1 Ma	482 ± 2 Ma

effects of subduction zone metamorphism has also been attempted. U-Pb dating of zircon from a block of retrogressed eclogite at Attunga (Figure 1b) yielded an age of 536 + 18 Ma [*Fanning et al.*, 2002]. However, because magmatic zircon can survive eclogite facies metamorphism [e.g., *Rubatto et al.*, 1998] it remains unclear whether this age represents the timing of protolith crystallization or metamorphism. The exhumation of rocks containing blueschist facies mineral assemblages during the early Ordovician (480–465 Ma) is based on K-Ar dating of phengite from samples at Glenrock and Pigna Barney (Figure 1b) [*Fukui et al.*, 1995, 2012]. Again, the relevance of this age is uncertain due to the potential problems associated with excess argon in high-pressure metamorphic rocks [*Kelley*, 2002].

3. Samples

Four samples recording the effects of subduction zone metamorphism were collected from key localities along the Peel-Manning Fault System (Table 1). These samples are as follows: (i) sample AT2 is from Attunga and preserves a retrogressed eclogite facies mineral assemblage (Figure 2a); (ii) sample 7936 from Glenrock and samples 47302 and PB3C from Pigna Barney record blueschist facies assemblages (Figure 2b). All of the samples come from allochthonous blocks contained within serpentinite matrix mélange. Extremely poor bedrock exposures at the Attunga locality prevent documentation of the stratigraphic and structural relationships between the eclogite block, serpentinite matrix mélange, and hosting fault system. At better exposed localities to the north in the Woodsreef and Upper Bingara regions (Figure 1b), a dismembered west facing sequence of schistose serpentinite, layered wehrlite-clinopyroxenite, layered gabbro, intrusive gabbro-dolerite, and chert has been identified [*Blake and Murchey*, 1988]. Given the widely acknowledged inference that the exotic blocks are located in the serpentinized harzburgite layer of the original ophiolite sequence [*Blake and Murchey*, 1988], we suggest that the eclogite block at Attunga is located in the basal part of a west facing ophiolite sequence. Sample AT2 comprises thoroughly retrogressed patches of a chlorite and actinolite assemblage that is dispersed among higher-grade, garnet-bearing parts of the rock. The sample lacks internal foliation or microstructure in groundmass minerals and shows no evidence of ductile deformation. Samples 7936, PB3C, and 47302 were collected from meter-scale blocks of lawsonite-bearing blueschist at Glenrock and Pigna Barney (Figures 1b and 2b). Coherent structural relationships between the metamorphic blocks and encompassing serpentinite are lacking at both Glenrock and Pigna Barney, with structural fabrics in the serpentinite wrapping around the competent high-pressure metamorphic knockers. The degree of internal deformation of the lawsonite-blueschist blocks is variable, ranging from the development of a disjunctive foliation in sample 7936 to a fine-grained continuous foliation that is crenulated in sample 47302. Consequently, it is difficult to reconcile the timing of deformation in the tectonic blocks with finite strain patterns recorded by the encompassing serpentinite matrix mélange.

4. Methods

Bulk rock and mineral composition data were collected from the samples to (i) discriminate the tectonic setting of protolith formation, (ii) characterize the main metamorphic mineral phases, and (iii) determine mineral compositions and end-member activities for thermobarometry. For samples AT2, 47302, and PB3C, major and trace elements were determined by XRF at The University of Newcastle (SPECTRO X-LAB 2000) and inductively coupled mass spectrometry (ICP-MS) at Genalysis Laboratory Services, Adelaide. For sample 7936, major elements were determined by XRF at The University of Newcastle and rare earth element (REE), Th, Ta, and U determined by neutron activation analysis at Becquerel Laboratories, Lucas Heights. The bulk rock

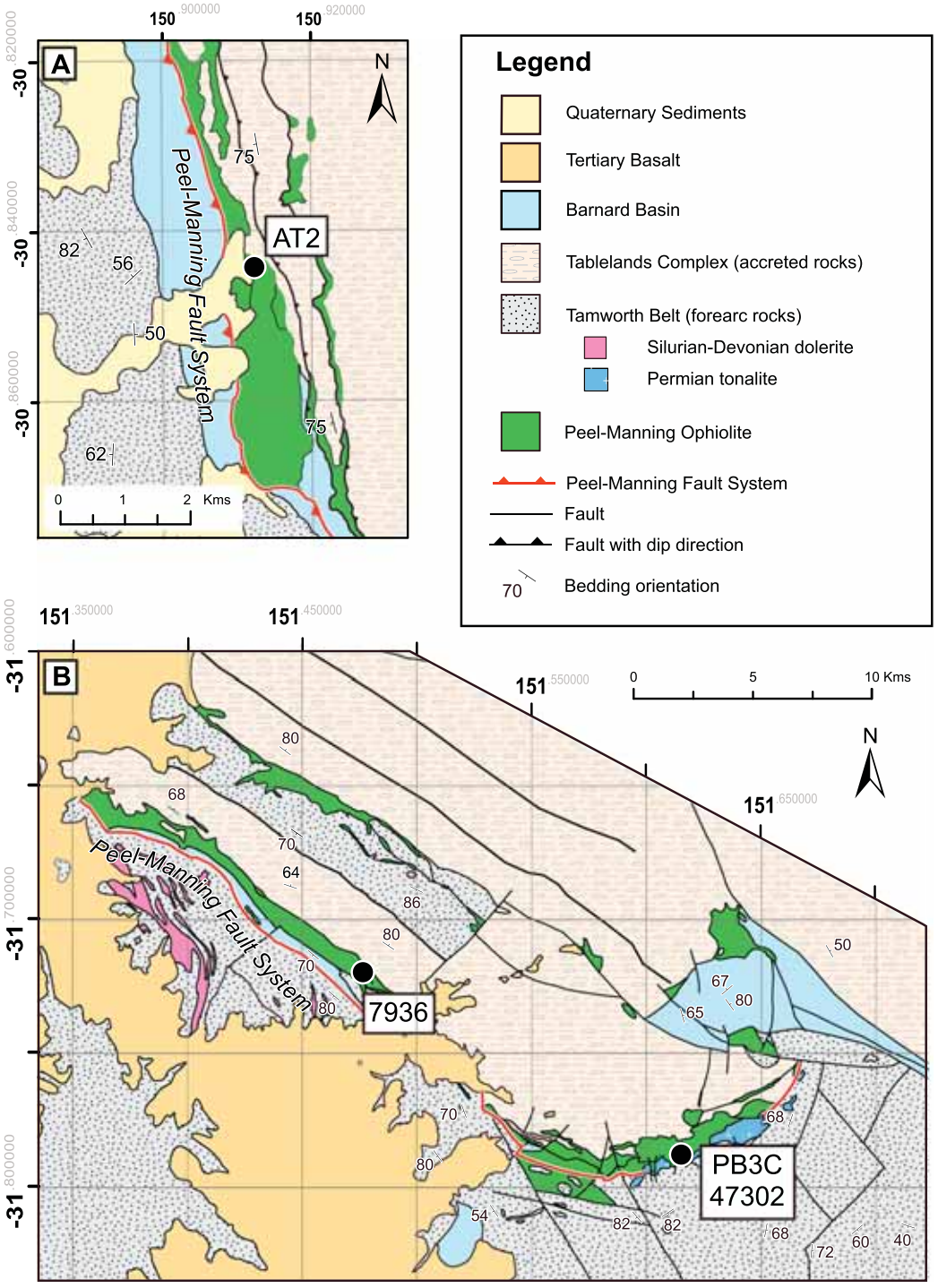

Figure 2. Geological maps of the sample localities. (a) Geological map of the Attunga region showing the location of eclogite sample AT2. (b) Geological map of the Glenrock and Pigna Barney regions showing the locations of samples 7936, PB3C, and 47302. Maps are extracted from the Geological Survey of NSW Seamless Statewide Geology Geodatabase [*Colquhoun et al.*, 2015].

compositional data are provided in Table 2. Mineral compositions were determined on a PHILIPS XL30 scanning electron microscope with attached IS200 energy-dispersive spectrometer at The University of Newcastle, Australia. Operating conditions involved a counting time of 60 s, an average beam diameter of 0.5 μm, and an accelerating voltage of 15 keV and 0.2 nA. Mineral composition data were collected as weight

Table 2. Bulk Composition of Samples Showing Major Element Concentrations as Oxide Percent and Trace Element Concentrations as Parts Per Million

	Sample			
	AT2	7936	47302	PB3C
	Major Elements			
SiO_2	46.7	57.66	48.99	51.54
TiO_2	1.21	0.34	3.37	1.76
Al_2O_3	15.2	15.64	13.47	13.57
Fe_2O_3	12.57	7.3	15.13	14.84
MnO	0.18	0.13	0.25	0.2
MgO	9.1	4.33	6.91	6.14
CaO	12.66	5.92	7.13	7.28
Na_2O	2.18	2.2	3.95	4.35
K_2O	0.1	3.4	0.49	0.18
P_2O_5	0.11	0.38	0.3	0.12
Total	100.01	97.32	99.99	99.98
	Trace Elements			
Ba	138.9	930	106.5	43.3
Be	nd	-	1.1	0.7
Ce	7.9	46	25.6	14.2
Cr	300	277	48	62
Cs	0.94	-	0.89	0.46
Cu	94	-	94	54
Dy	4.53	-	6.98	6.25
Er	2.87	-	4.12	3.9
Eu	1.04	1.21	1.91	1.54
Ga	16.9	16	20.8	17.9
Gd	3.69	3.3	6.41	5.53
Hf	2	1.5	4.4	3.2
Ho	0.96	0.4	1.41	1.29
La	2.7	25	10.3	5.3
Lu	0.41	0.2	0.6	0.57
Mo	0.3	-	0.8	0.1
Nb	3.7	7	15.1	3.6
Nd	7.6	21	18.5	12.2
Ni	104	25	18	55
Pr	1.37	-	3.86	2.34
Rb	4.4	74	7.6	10.8
Sm	2.82	4.1	5.66	4.38
Sr	115	-	133.1	59.3
Ta	0.3	0.3	1	0.3
Tb	0.65	-	1.05	0.9
Th	0.3	5.1	1.08	0.44
Tl	nd.	-	0.06	0.02
Tm	0.46	-	0.61	0.6
U	nd.	2.2	0.27	0.24
V	321	141	409	405
Y	29.9	15	41.5	38.1
Yb	2.77	1.22	3.62	3.68
Zn	84	-	115	114
Zr	66	90	145	96
La/Sm	0.96	6.10	1.82	1.21

percent oxides, and ideal stoichiometric formulae calculated on a per formula unit (pfu) basis. Standards of known elemental composition were measured at the beginning and end of each analytical session to ensure the accuracy of measured data and to monitor for machine drift. Representative mineral compositional data are given in Tables 3 and 4. Conventional and optimal thermobarometry were carried out using these data and numerous techniques (see section 5.3) [*Brown*, 1977; *Holland*, 1980; *Powell and Holland*, 1994; *Ernst and Liu*, 1998; *Krogh-Ravna*, 2000].

For U-Pb age determination, zircons were separated from sample AT2 after rock crushing using conventional heavy liquid and magnetic properties. The grains were mounted in epoxy resin and polished down to expose the near equatorial section. Cathodoluminescence (CL) investigation was carried out on a HITACHI S2250N scanning electron microscope (SEM) supplied with an ellipsoidal mirror for CL at the Research School of Earth Sciences, The Australian National University (RSES-ANU) in Canberra, Australia. Operating conditions for the SEM were 15 kV/60 μA and 20 mm working distance. The zircons were then analyzed for U, Th, and Pb using the sensitive high-resolution ion microprobe (SHRIMP II) at the RSES-ANU. Instrumental conditions and data acquisition are described by *Williams* [1998]. The data were collected in sets of six scans throughout the masses, and a reference zircon was analyzed each fourth analysis. U-Pb data were collected in one analytical session having a 2 sigma calibration error of 1.0%, which was propagated to single analyses. The measured $^{206}Pb/^{238}U$ ratio was corrected using reference zircon from the Temora granodiorite (417 Ma) [*Black et al.*, 2003]. The fraction of nonradiogenic ^{206}Pb (f_{206}) was calculated from the measured $^{207}Pb/^{206}Pb$ ($^{7/6}R_m$) and the nonradiogenic $^{207}Pb/^{206}Pb$ ($^{7}R_c$) according to *Williams* [1998], i.e., $f_{206} = (^{7/6}R_m - {}^{7/6}R^*)/(^{7/6}R_c - {}^{7/6}R^*)$, where $^{7/6}R^*$ is the expected radiogenic $^{207}Pb/^{206}Pb$ assuming concordance at the approximate age of the sample. The $^{7}R_c$ composition was assumed to be that predicted by the *Stacey and Kramers* [1975] model. Age calculations were achieved using the software Squid 1 and Isoplot/Ex [*Ludwig*, 2003]. Average ages are quoted at the 95% confidence level with uncertainties forced to at least 1% to account for external errors.

Table 3. Mineral Compositional Data From Eclogite Sample AT2[a]

	Phase									
	Garnet									
	Texture									
	Core	Rim	omp	di	gl	fe-hb	act	Albite	Epidote	Chlorite
SiO_2	37.16	39.20	54.44	53.40	56.77	42.07	55.18	68.05	38.13	26.71
TiO_2	0.11	0.08	0.22	0.25	0.04	0.20	0.06	0.05	0.14	0.09
Al_2O_3	20.92	21.82	7.84	8.13	10.91	12.90	1.61	19.31	25.16	19.39
Cr_2O_3	0.00	0.00	0.00	0.05	0.02	0.02	0.00	0.06	0.11	0.11
FeO	26.32	21.78	9.42	5.00	10.80	19.01	12.10	0.22	10.15	27.06
MnO	3.36	0.31	0.25	0.07	0.02	0.30	0.05	0.02	0.00	0.23
MgO	2.01	7.83	7.20	10.55	8.86	7.51	15.23	0.07	0.12	14.32
CaO	10.27	9.22	14.21	18.74	0.43	11.76	11.01	0.06	23.51	0.14
Na_2O	0.00	0.02	6.36	3.42	7.27	2.45	1.15	11.35	0.00	0.26
K_2O	0.00	0.04	0.00	0.00	0.00	0.67	0.14	0.00	0.00	0.02
Total	100.15	100.30	99.94	99.61	95.12	96.89	96.53	99.19	97.32	88.33
Si	2.95	2.98	1.98	1.94	8.03	6.45	7.97	2.99	3.00	2.82
Ti	0.01	0.01	0.01	0.01	0.00	0.02	0.01	0.00	0.01	0.01
Al	1.96	1.96	0.34	0.35	1.82	2.33	0.27	1.00	2.33	2.41
Cr	0.00	0.00	0.00	0.00	0.00	0.00	0.00	0.00	0.01	0.01
Fe^{3+}	0.13	0.07	0.15	0.00	0.00	0.00	0.01	0.01	0.62	0.00
Fe^{2+}	1.62	1.32	0.14	0.15	1.28	2.44	1.46	0.00	0.04	2.39
Mn	0.23	0.02	0.01	0.00	0.00	0.04	0.01	0.00	0.00	0.02
Mg	0.24	0.89	0.39	0.57	1.87	1.72	3.28	0.01	0.01	2.25
Ca	0.87	0.75	0.55	0.73	0.07	1.93	1.71	0.00	1.98	0.02
Na	0.00	0.00	0.45	0.24	1.99	0.73	0.32	0.97	0.00	0.05
K	0.00	0.00	0.00	0.00	0.00	0.13	0.03	0.00	0.00	0.00
Sum	8.00	8.00	4.00	4.00	15.05	15.79	15.06	4.98	8.01	9.99
Jadeite			30	25						

[a]Abbreviations: omp = omphacite; di = diopside; gl = glaucophane; fe-hb = ferroan hornblende; and act = actinolite. Jadeite = Na/(Na + Ca).

Trace elements of individual zircon grains were determined by laser ablation ICP-MS at the RSES-ANU (Table 5). The instrument includes an ANU "HelEx" laser ablation cell built to receive a pulsed 193 nm wavelength ArF excimer laser with 100 mJ output energy at a repetition rate of 5 Hz and coupled to an Agilent 7700s quadrupole ICP-MS. The instrument was tuned for maximum sensitivity and minimum production of molecular species, maintaining ThO^+/Th^+ at $<0.5\%$. The laser was operated in drilling mode with a spot size of 27 μm. Total analysis time was 60 s, the first 25 s of which was background acquisition prior to ablation. Synthetic glass NIST 612 was used for external calibration, and reference values were taken from *Pearce et al*. [1997]. Internal standards were SiO_2 of 32.45 wt %. The BCR-2G natural glass was used as a secondary standard to monitor accuracy, which was within 10% of the reference value. Data evaluation was achieved using an internal spreadsheet compiled at RSES-ANU. Chondrite values for normalization are from *McDonough and Sun* [1995].

$^{40}Ar/^{39}Ar$ isotope analyses were carried out on phengite from lawsonite-blueschist samples PB3C and 7936. Samples were analyzed by conventional furnace step-heating techniques at the University of Melbourne, following the published analytical procedures of *Phillips et al*. [2007]. The data yielded from these analyses did not meet the requirements for the calculation of plateau ages, which are defined as (i) incorporating more than three contiguous gas fractions, (ii) together representing more than 50% of the total ^{39}Ar released, and (iii) having ages on individual temperature steps within 2 sigma error of the mean age [*Fleck et al*., 1977]. As a result, weighted mean ages were calculated using the Isopleth software [*Ludwig*, 2003]. Owing to the potential for contamination by excess argon in high-pressure rocks [*Kelley*, 2002], a two-increment step-heating laser approach was also employed on single grains of phengite. The laser analyses were again carried out at The University of Melbourne, employing the analytical procedures outlined by *Phillips and Harris* [2008]. This approach was used to screen for any significant intrasample variance in argon content that may be an artifact of (i) multiple generations of mica growth or (ii) varied degrees of isotopic resetting or

Table 4. Mineral Compositional Data From Blueschist Samples 7936, PB3C, and 47302[a]

	Sample														
	7936						PB3C			47302					
	Texture														
	Inclusion	Core	Foliation (early)	Early	Foliation	Foliation	Inclusion	Foliation	Foliation	Peak	Peak	Foliation	Foliation	Foliation (early)	Early
	Phase														
	ph	act-hb	mg-hb	ep	gl	ph	ph	ph	gl	g	g	ph	gl	mg-hb	ep
SiO_2	53.91	49.31	42.79	37.73	56.37	47.59	54.95	46.56	55.95	36.77	36.69	53.04	55.06	44.63	38.53
TiO_2	0.12	0.26	0.76	0.01	0.25	0.88	0.28	0.43	0.08	0.21	0.19	0.10	0.00	0.53	0.00
Al_2O_3	21.00	6.40	11.75	25.49	9.31	27.19	21.38	27.14	11.28	20.46	20.36	19.75	8.00	14.17	29.51
Cr_2O_3	0.09	0.10	0.07	0.01	0.02	0.04	0.07	0.02	0.00	0.03	0.05	0.06	0.00	0.11	0.04
FeO	2.64	12.83	12.92	10.07	13.33	3.95	3.01	3.36	13.08	21.92	24.94	4.44	21.32	15.67	4.61
MnO	0.00	0.37	0.29	0.30	0.11	0.01	0.11	0.05	0.09	7.95	6.11	0.16	0.14	0.02	0.75
MgO	4.76	13.27	12.57	0.15	8.77	2.84	5.49	2.70	7.77	1.04	1.24	4.60	5.28	9.51	0.10
CaO	0.13	9.24	11.04	22.83	0.97	0.04	0.14	0.07	0.46	11.09	9.49	0.05	1.43	9.57	23.52
Na_2O	0.00	2.14	1.98	0.00	6.81	0.13	0.00	0.33	7.12	0.00	0.00	0.00	6.51	3.50	0.00
K_2O	9.79	0.20	1.23	0.02	0.01	9.51	11.15	9.56	0.05	0.00	0.03	10.23	0.01	0.26	0.00
Totals	92.44	94.12	95.40	96.61	95.95	92.18	96.58	90.22	95.88	99.47	99.10	92.43	97.75	97.97	97.06
Si	3.69	7.34	6.44	2.98	7.99	3.28	3.64	3.28	7.93	2.95	2.97	3.68	7.96	6.54	3.00
Ti	0.01	0.03	0.09	0.00	0.03	0.05	0.01	0.02	0.01	0.01	0.01	0.01	0.00	0.06	0.00
Al	1.69	1.12	2.08	2.38	1.56	2.21	1.67	2.26	1.89	1.94	1.94	1.62	1.36	2.45	2.71
Cr	0.01	0.01	0.01	0.00	0.00	0.00	0.00	0.00	0.00	0.00	0.00	0.00	0.00	0.01	0.00
Fe^{3+}	0.00	0.33	0.32	0.66	0.21	0.16	0.00	0.11	0.09	0.13	0.11	0.00	0.32	0.19	0.26
Fe^{2+}	0.15	1.27	1.31	0.01	1.37	0.07	0.17	0.09	1.46	1.35	1.58	0.26	2.26	1.73	0.04
Mn	0.00	0.05	0.04	0.02	0.01	0.00	0.01	0.00	0.01	0.54	0.42	0.01	0.02	0.00	0.05
Mg	0.49	2.94	2.82	0.02	1.85	0.29	0.54	0.28	1.64	0.13	0.15	0.48	1.14	2.08	0.01
Ca	0.01	1.47	1.78	1.93	0.15	0.00	0.01	0.01	0.07	0.96	0.82	0.00	0.22	1.50	1.96
Na	0.00	0.62	0.58	0.00	1.87	0.02	0.00	0.05	1.96	0.00	0.00	0.00	1.83	0.99	0.00
K	0.85	0.04	0.24	0.00	0.00	0.84	0.94	0.86	0.01	0.00	0.00	0.91	0.00	0.05	0.00
Sum	6.89	15.34	15.79	8.00	15.11	6.92	6.99	6.96	15.09	8.00	8.00	6.96	15.22	15.67	8.03

[a]Abbreviations: ph = phengite, act-hb = actinolitic-hornblende, gl = glaucophane, mg-hb = magnesiohornblende, ep = epidote, g = garnet.

excess argon contamination within individual grains. Using the single-grain laser approach, spurious isotopic results from a single-grain analysis can be removed from the mean age calculations, again carried out using the Isoplot software [*Ludwig*, 2003]. In order to integrate our $^{40}Ar/^{39}Ar$ age data with the *P-T* histories, we assume a temperature of 350°C for the closure of argon diffusion in white mica [*Hames and Bowring*, 1994].

5. Results

5.1. Petrography

Eclogite sample AT2 comprises large (<1 cm), shattered porphyroblasts of garnet that are imbedded in a matrix of diopside, actinolite, chlorite, albite, and titanite (Figure 3a). Garnet is subidioblastic in shape and contains small inclusions (<10 μm) of glaucophane, lawsonite, omphacite, rutile, epidote, and quartz. The inclusion assemblage occupies intact fragments of garnet, with cracks filled with albite and chlorite. The inclusion-rich cores are encased by thin (<2 mm) inclusion-free rims. Reaction textures and compositional zoning away from the garnet-diopside interfaces are lacking (Figure 3b), which we tentatively interpret to represent equilibrium between these phases. Amphibole in the groundmass is dominantly actinolite, yet grains of actinolite comprising relicts of sodic amphibole and ferroan hornblende are present (Figure 3c). Retrograde minerals in the groundmass include chlorite and albite, all of which lack preferred tectonic alignment.

The mineral assemblage in the lawsonite-blueschist samples 7936 and PB3C is made up of white mica, amphibole, lawsonite, epidote, titanite in a groundmass of albite, and quartz. A well-developed foliation consists of aligned grains of amphibole, white mica, lawsonite, and titanite (Figure 3d). Two contrasting types of compositional zoning are evident in amphibole, which can be summarized as (i) a patchy to complete

AGU Tectonics

10.1002/2015TC003920

Table 5. LA-ICP-MS Trace Element Analyses of Zircon Grains From Eclogite Sample AT2

	Spot Name															
	AT2-15A	AT2-21	AT2-5	AT2-24	AT2-33	AT2-4	AT2-11	AT2-12	AT2-1	AT2-7	AT2-30	AT2-16	AT2-14	AT2-9A	AT2-18	AT2-8
	CL Domain															
	CL Dark Core	CL Dark Core	Rim	Rim	Rim	Rim	Core Sector	Rim Sector	Core	Rim	Rim	Rim	Rim	Core	Rim	Rim
P	471.6	129.6	55.4	63.5	54.3	57.3	64.9	64.9	101.5	53.8	56.0	56.0	61.2	65.0	57.0	88.6
Ti	30.6	11.63	2.23	4.20	3.04	5.58	3.28	5.04	5.26	13.69	11.07	9.98	2.88	2.97	8.69	3.76
Sr	1.3	0.19	0.15	0.14	0.13	0.31	0.13	0.15	0.20	0.14	0.16	0.16	0.14	0.09	0.14	0.16
Y	1974.2	331.76	17.14	28.71	37.75	131.08	34.98	39.99	207.93	24.31	38.70	44.88	31.73	31.20	38.45	62.80
Nb	2.2	1.46	0.43	0.39	0.43	0.42	0.42	0.42	0.43	0.38	0.40	0.41	0.39	0.40	0.40	0.51
La	2.46	0.015	<0.003	<0.003	<0.003	<0.003	<0.003	0.004	<0.003	<0.003	0.003	<0.003	<0.003	<0.003	<0.003	0.003
Ce	14.6	1.91	0.007	0.022	0.012	0.041	0.006	0.027	0.178	0.086	0.021	0.020	0.006	0.043	0.014	0.083
Pr	2.6	0.02	<0.003	<0.003	<0.003	<0.003	<0.003	<0.003	0.003	0.008	<0.003	<0.003	<0.003	0.003	<0.003	<0.003
Nd	28.7	0.32	<0.006	<0.006	<0.006	0.017	0.012	0.013	0.047	0.094	0.007	<0.006	<0.006	<0.006	0.025	<0.006
Sm	20.2	0.90	<0.02	0.05	0.03	0.05	<0.02	0.05	0.28	0.31	0.04	0.02	<0.02	0.07	0.04	0.18
Eu	8.5	0.71	0.01	0.06	0.01	0.07	0.01	0.04	0.20	0.15	0.03	0.03	0.01	0.08	0.04	0.19
Gd	61.2	6.09	0.07	0.71	0.26	0.65	0.19	0.34	2.74	1.05	0.39	0.36	0.24	0.86	0.43	1.54
Tb	11.8	1.86	0.04	0.31	0.17	0.44	0.08	0.17	1.23	0.29	0.22	0.18	0.15	0.36	0.18	0.51
Dy	124.7	23.64	0.89	3.07	2.77	7.86	1.71	2.19	16.01	2.46	2.91	2.76	2.36	3.46	2.53	5.10
Ho	44.6	8.39	0.38	0.74	0.97	3.22	0.80	0.99	5.68	0.61	0.96	1.12	0.81	0.83	0.96	1.48
Er	209.9	40.63	2.16	2.10	4.00	14.60	4.17	5.74	26.17	1.99	4.26	5.75	3.56	2.52	4.34	7.24
Tm	48.5	9.88	0.60	0.32	0.77	3.17	0.93	1.58	6.08	0.36	0.84	1.30	0.77	0.41	0.89	1.64
Yb	509.8	105.95	5.85	2.30	6.71	27.91	8.04	16.62	64.36	2.88	7.45	11.76	6.38	2.96	7.93	17.08
Lu	117.2	23.51	1.13	0.37	1.12	4.32	1.24	3.56	11.72	0.45	1.22	2.07	1.05	0.46	1.34	3.15
Hf	8425	8793	10806	10387	11537	10317	10227	10759	8799	10386	10649	10850	10911	8812	10895	10004
Ta	1.7	1.04	0.05	0.05	0.05	0.05	0.05	0.05	0.06	0.04	0.05	0.04	0.06	0.06	0.04	0.06
Pb	4.3	1.92	<0.02	<0.02	<0.02	<0.02	<0.02	0.12	0.09	0.14	<0.02	<0.02	<0.02	<0.02	<0.02	<0.02
Th	95.1	45.48	0.00	0.04	0.02	0.06	0.01	0.09	1.76	0.18	0.09	0.13	0.02	0.06	0.11	0.03
U	1265	647.62	0.12	5.21	1.64	2.38	0.30	2.52	13.63	4.67	2.50	2.34	0.97	11.19	2.00	25.12
Th/U	0.08	0.07	0.02	0.01	0.01	0.03	0.04	0.03	0.13	0.04	0.04	0.06	0.02	0.01	0.05	0.00
Eu/Eu^{*a}	0.68	0.69		0.58	0.31	0.68		0.72	0.45	0.73	0.50	0.52		0.60	0.64	0.74
$Lu_N/Gd_N{}^b$	15.5	31.2	130.3	4.2	35.5	53.6	52.0	85.4	34.6	3.5	25.5	46.3	35.9	4.3	25.3	16.5
$Lu_N/Dy_N{}^b$	9.4	9.9	12.8	1.2	4.0	5.5	7.2	16.2	7.3	1.8	4.2	7.5	4.4	1.3	5.3	6.2
Lu/Hf × 1000	13.9	2.67	0.10	0.04	0.10	0.42	0.12	0.33	1.33	0.04	0.11	0.19	0.10	0.05	0.12	0.31
Pb/U Age	474	481		399	421	422	446	451	473	478	482	484	484	486	488	494
±1 sigma	2	1		11	23	39	39	18	7	19	26	17	27	5	20	6

[a] $Eu^* = (Gd_N + Sm_N)/2$.
[b] N = element normalized to chondrite abundance.

AGU Tectonics

10.1002/2015TC003920

Table 5. (continued)

Spot Name																	
AT2-3	AT2-35	AT2-9	AT2-1A	AT2-17	AT2-17	AT2-6	AT2-10	AT2-13	AT2-32	AT2-29	AT2-28	AT2-27	AT2-25	AT2-31	AT2-19	AT2-34	AT2-22
CL Domain																	
Core Sector	Rim	Rim	Rim + Core	Core Sector	Core Sector	Core Sector	Core	Core	Core sector	Rim	Rim	Rim	Rim	Rim	Rim	Rim	Rim
56.7	62.8	115.0	88.8	54.0	51.2	70.8	60.7	67.0	57.5	74.3	57.2	69.3	49.2	55.1	72.8	51.8	56.0
3.34	3.64	8.88	5.20	4.31	4.81	8.09	4.62	4.62	4.44	5.86	3.09	3.12	4.41	3.16	9.53	5.20	5.90
0.12	0.16	0.44	0.19	0.13	0.12	0.13	0.12	0.17	0.14	0.27	0.15	0.12	0.18	0.12	0.20	0.14	0.20
103.99	31.36	449.63	159.65	33.85	26.78	72.34	89.78	116.24	90.02	146.55	54.15	57.18	28.41	27.08	57.21	31.00	47.72
0.38	0.40	0.66	0.51	0.38	0.40	0.43	0.41	0.43	0.42	0.54	0.43	0.46	0.41	0.38	0.45	0.42	0.45
<0.003	0.003	0.002	0.02	<0.003	<0.003	<0.003	<0.003	<0.003	<0.003	0.01	<0.003	<0.003	0.003	<0.003	0.025	<0.003	0.006
0.016	0.010	0.085	0.146	0.050	0.050	0.081	0.029	0.035	0.022	0.075	0.035	0.009	0.025	0.017	0.105	0.027	0.030
<0.003	0.003	<0.003	0.017	<0.003	<0.003	<0.003	<0.003	<0.003	<0.003	<0.003	<0.003	<0.003	<0.003	<0.003	0.023	<0.003	<0.003
<0.006	0.013	<0.006	0.086	0.035	0.051	0.017	0.010	0.015	<0.006	<0.006	<0.006	0.007	<0.006	0.006	0.190	0.023	0.017
0.06	0.06	0.08	0.18	0.05	0.08	0.04	0.19	0.04	<0.02	0.04	0.07	<0.02	0.02	0.03	0.18	0.08	<0.02
0.05	0.04	0.15	0.12	0.05	0.07	0.06	0.24	0.04	0.03	0.06	0.08	0.02	0.03	0.04	0.08	0.03	0.06
1.11	0.32	2.58	1.69	0.38	0.41	0.55	2.78	0.64	0.47	0.81	1.09	0.19	0.22	0.46	0.84	0.40	0.59
0.63	0.13	1.46	0.73	0.14	0.12	0.19	1.12	0.33	0.25	0.35	0.42	0.12	0.12	0.18	0.30	0.20	0.27
8.59	2.11	26.30	10.13	1.86	1.46	3.44	10.83	6.59	4.86	6.44	5.36	2.69	1.73	2.12	3.67	2.46	3.70
2.58	0.77	11.73	3.97	0.81	0.62	1.68	2.40	2.95	2.32	3.75	1.46	1.38	0.70	0.74	1.38	0.80	1.18
9.43	3.75	50.38	21.14	3.78	3.34	10.04	6.88	14.90	12.90	28.83	4.42	9.04	3.43	2.72	6.58	3.13	4.84
1.67	0.79	8.77	5.06	0.80	0.75	2.72	1.09	3.47	3.07	9.95	0.70	2.58	0.81	0.48	1.44	0.63	0.90
13.80	7.18	66.02	51.77	6.78	6.91	27.05	7.76	31.06	30.57	132.72	5.20	29.51	6.79	4.36	12.57	5.27	7.57
1.98	1.25	11.70	11.50	1.10	1.18	5.10	1.13	5.56	5.68	30.95	0.77	6.52	1.15	0.76	2.31	0.90	1.42
9455	10250	9427	9888	10776	11275	9881	9611	10210	9807	11170	10535	9096	11185	11110	11323	11423	11448
0.05	0.05	0.08	0.10	0.05	0.05	0.05	0.04	0.05	0.04	0.10	0.05	0.09	0.05	0.05	0.06	0.05	0.05
<0.02	<0.02	<0.02	<0.02	<0.02	<0.02	<0.02	0.03	0.10	0.02	0.08	0.07	<0.02	0.05	<0.02	0.04	<0.02	0.78
0.03	0.07	0.33	0.37	0.04	0.04	0.21	0.06	0.10	0.02	0.74	0.06	0.04	0.07	0.04	0.22	0.10	0.06
1.26	1.72	25.17	19.59	0.73	0.78	2.06	4.28	2.72	0.73	11.48	4.75	7.18	2.52	1.59	7.09	1.32	2.44
0.03	0.04	0.01	0.02	0.05	0.05	0.10	0.01	0.04	0.03	0.06	0.01	0.01	0.03	0.03	0.03	0.07	0.03
0.30	0.61	0.40	0.45	0.87	1.02	0.73	0.56	0.35		0.50	0.49		0.72	0.56	0.54	0.48	
14.4	31.1	36.7	54.9	23.6	23.0	75.7	3.3	70.2	98.7	307.9	5.8	281.1	42.3	13.3	22.3	18.1	19.6
2.3	5.9	4.4	11.4	5.9	8.1	14.9	1.0	8.4	11.7	48.1	1.4	24.2	6.7	3.6	6.3	3.7	3.8
0.21	0.12	1.24	1.16	0.10	0.10	0.52	0.12	0.54	0.58	2.77	0.07	0.72	0.10	0.07	0.20	0.08	0.12
496	503	505	507	508	508	509	511	511	515	517	520	520	522	529	533	542	600
30	13	7	8	40	40	21	27	16	31	11	14	10	17	23	12	24	30

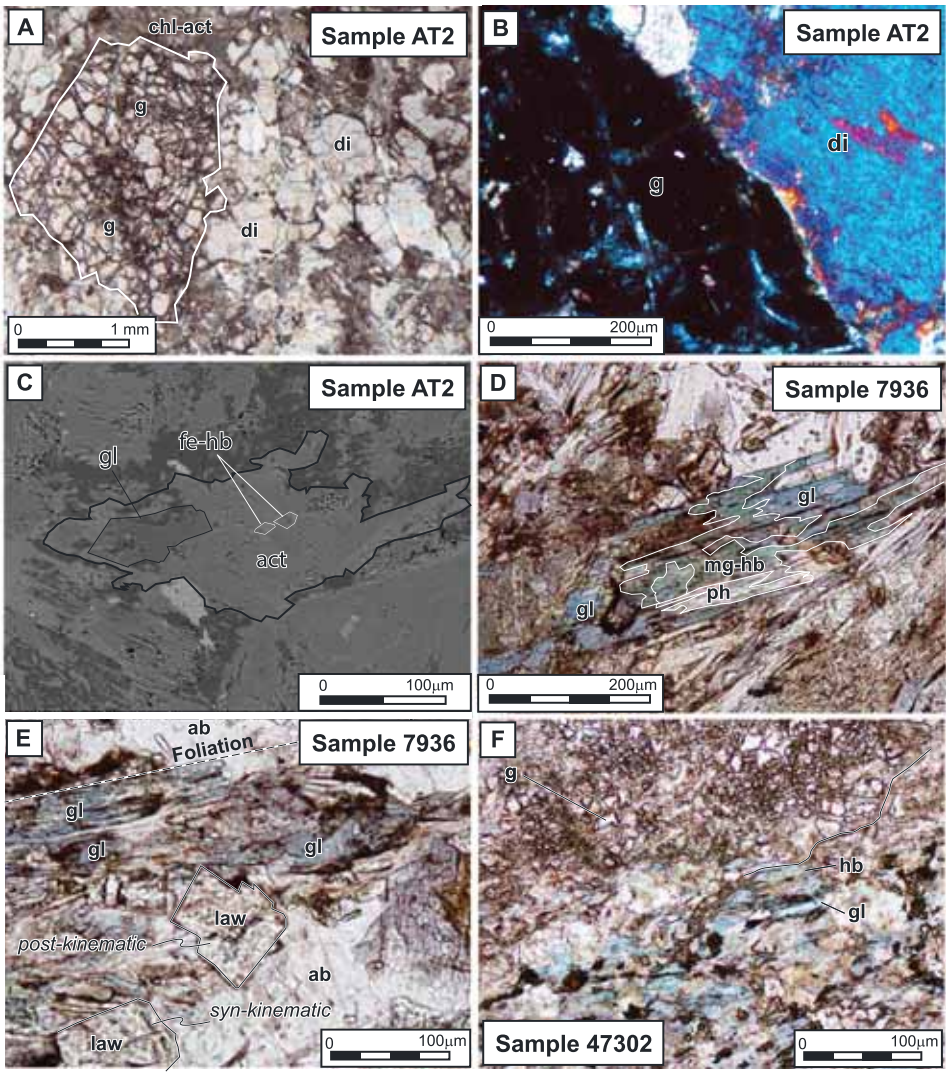

Figure 3. Photomicrographs showing key petrographic relationships between mineral phases. (a) Sample AT2: shattered peak *P* garnet porphyroblasts (g) that are surrounded by retrograde clinopyroxene (diopside = di), actinolite (act), chlorite (chl), and albite. (b) Sample AT2: close-up of garnet (g)-diopside (di) interface showing the lack of reaction textures. (c) Sample AT2: back-scattered image of a zoned amphibole in the groundmass showing relicts of glaucophane (gl) and ferroan hornblende (fe-hb) in actinolite (act). (d) Sample 7936: magnesiohornblende (mg-hb) partially replaced by glaucophane (gl) that defines the foliation in association with phengite (ph). (e) Sample 7936: close-up of the foliation comprising glaucophane (gl) and synkinematic to postkinematic lawsonite (law) surrounded by albite (ab). (f) Sample 47302: highly fragmented garnet (g) that preserves a prekinematic textural relationship with amphibole defined by early formed magnesiohornblende (green) overprint by glaucophane (blue).

replacement of calcic-amphibole by sodic-amphibole in amphibole grains that define the foliation (Figure 3c) and (ii) a core-rim zoning between early formed cores of calcic-amphibole and thin rims ($<$50 μm) of sodic-amphibole. Lawsonite can be elongated and aligned with the dominant foliation, as well as equant and overgrowing the foliation, signifying a synkinematic to postkinematic relationship (Figure 3e). In addition to the laths of white mica that define the foliation, small white mica inclusions are located within the amphibole defining the foliation. Epidote shows ragged grain boundaries, indicating that it probably formed prior to the amphibole, white mica, and lawsonite that define the foliation. Lawsonite-blueschist sample 47302 comprises a similar mineral assemblage to samples 7936 and PB3C, with amphibole, white mica, lawsonite, and titanite defining a well-developed foliation. Zoning in the amphibole is again defined by an early formed calcic-amphibole rimmed or partly replaced by

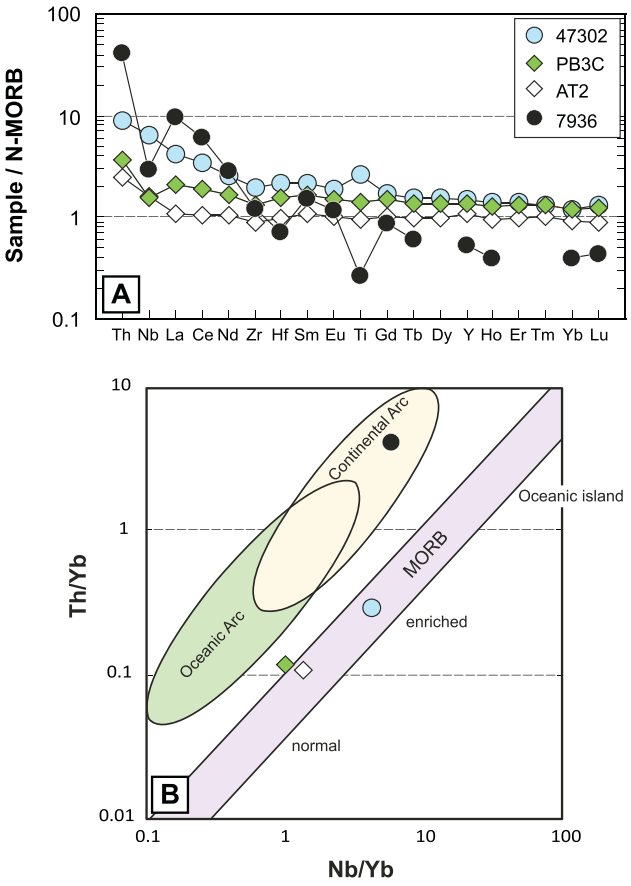

Figure 4. (a) Rock/N-MORB plot. Normalizing values are from *Sun and McDonough* [1989]. Trace elements known to be highly mobile during metamorphism (i.e., Sr and Ba) have been excluded from the plot. Note the slight enrichment of Th and Nb in samples 47302, PB3C, and AT2 relative to N-MORB. Based on their La/Sm values, samples AT2 and PB3C have affinities with transitional MORB. The La/Sm ratio for sample 47302 is consistent with derivation as an evolved MORB. The light REE enrichment, Nb depletion, and high Th content in sample 7936 is characteristic of magmas derived in a continental arc setting. (b) Th/Yb versus Nb/Tb tectonic discrimination plot after *Pearce* [2014]. Note that the same symbols from Figure 4a are used for each sample. Samples AT2, 47302, and PB3C plot in the normal- to enriched-MORB field of the diagram. Sample 7936 plots in the continental arc field of the diagram.

sodic-amphibole. In contrast to samples 7936 and PB3C, fragmented relicts of garnet are preserved in sample 47302 (Figure 3f). The foliation wraps around the relict garnet porphyroblasts, indicating that the garnet formed earlier than the blueschist facies assemblage.

5.2. Geochemistry

Trace elements known to be immobile during metamorphism were (i) normalized to normal mid-oceanic ridge basalt (N-MORB) [*Sun and McDonough*, 1989] and plotted on a standard spider diagram (Figure 4a) and (ii) plotted on the Th/Yb versus Nb/Yb discrimination diagram of *Pearce* [2014] (Figure 4b). On the spider diagram, samples AT2, 47302, and PB3C show an enrichment of Th and the light rare earth elements compared to N-MORB, as well as relatively flat heavy rare earth element patterns (Figure 4a). Nb is slightly enriched in sample 47302 and depleted in samples AT2 and PB3C (Figures 4a and 4b). Low La/Sm ratios recorded by samples AT2 (0.96) and PB3C (1.21) are characteristic of magmas derived in a transitional mid-oceanic ridge basalt (MORB) setting. The slight Nb depletion shown by samples AT2 and PB3C also indicates a possible back-arc basin affinity. Sample 47302 shows a higher La/Sm ratio (1.82) and has a more enriched-MORB magmatic affinity, which is also shown on the Th/Yb versus Nb/Yb plot (Figure 4b). Samples AT2, 47302, and PB3C are accordingly interpreted to have formed in a mid-ocean ridge setting. Sample 7936, in contrast, shows a significant depletion in Nb, Ti, and the heavy rare earth elements and a considerable enrichment in Th and the light rare earth elements (Figures 4a and 4b). These geochemical features are characteristic of andesitic magmas that form in continental arc settings [*Pearce*, 1983, 2014].

5.3. Mineral Compositions and Pressure-Temperature Calculations

Garnet analyses are normalized to 12 oxygens with Fe^{2+}/Fe^{3+} contents estimated using the AX program. The heavily fractured porphyroblasts of garnet in eclogite sample AT2 show discontinuous zoning with a grossular content decreasing toward the rim (core: $pyrope_8almandine_{55}grossular_{30}spessartine$, rim: $pyrope_{30}almandine_{44}grossular_{25}spessartine_1$; Table 3). Fragmented garnet in lawsonite-blueschist sample 47302 is a $pyrope_4almandine_{45}grossular_{32}spessartine_{18}$ solid solution that compares closely to the garnet cores analyzed in eclogite sample AT2 (Figure 5a and Table 4). Given the highly fragmented and pseudomorphed nature of garnet in sample 47302, the rim composition could not be analyzed. Pyroxene formulae are calculated by normalizing data to six oxygens, with Fe^{2+}/Fe^{3+} contents estimated by normalizing the

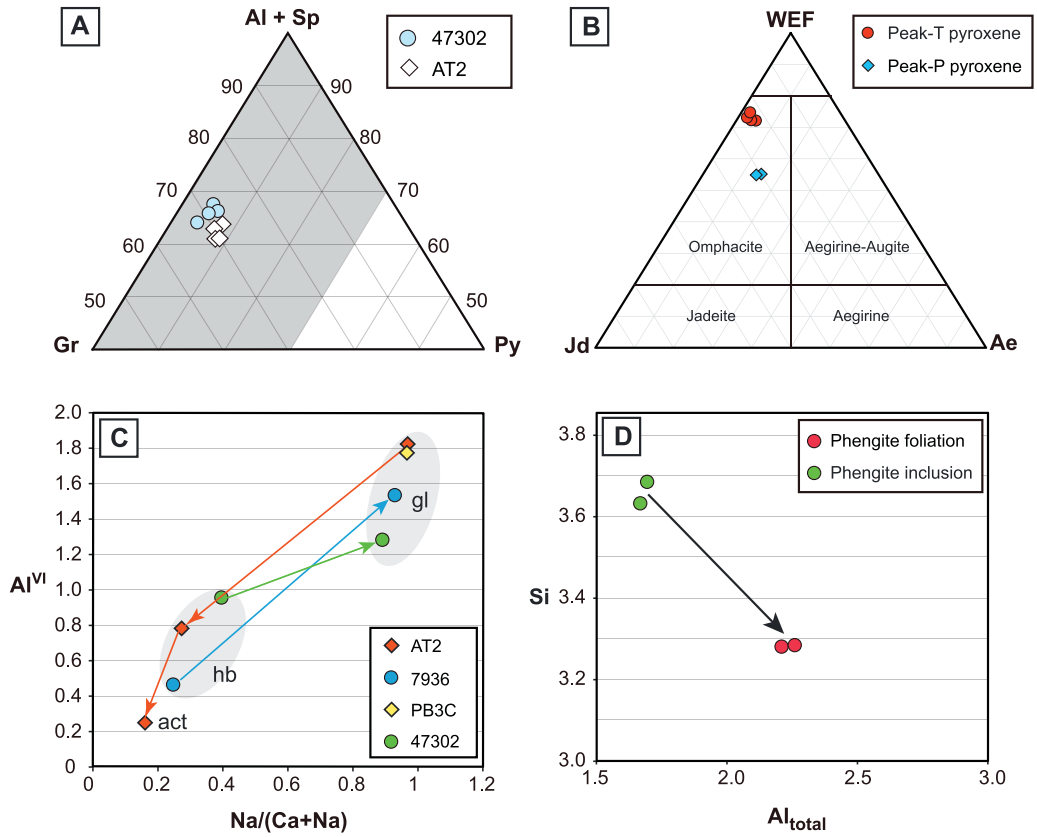

Figure 5. (a) Composition of garnet in samples AT2 and 47302 in terms of almandine (Al), spessartine (Sp), grossular (Gr), and pyrope (Py). Note the similarity of garnet chemistry in both samples and that they plot in the Group C eclogite field (grey shaded) of *Coleman et al.* [1965]. (b) WEF (wollastonite-enstatite-ferrosilite)-jadeite-aegirine ternary diagram showing the composition of high-pressure and high-temperature pyroxene in sample AT2. (c) Al^{VI} versus Na/(Ca + Na) plot of amphibole composition from all four samples. Arrows between data points represent the relative timing of amphibole growth. In sample AT2, early formed glaucophane (gl) is followed by higher-temperature hornblende (hb) and then actinolite (act). In samples 7936 and 47302, early formed magnesiohornblende is pseudomorphed or overgrown by glaucophane. (d) Si versus Al_{total} plot showing the contrasting pressure conditions of metamorphism during the growth of the early formed phengite inclusions compared to the foliation parallel phengite. Arrow shows the relative timing of mineral growth.

analyses to four cations. In eclogite sample AT2, pyroxene inclusions located in the garnet cores are enriched in Na and Al^{VI} and are omphacite in composition ($jadeite_{30}aegirine_{15}$wollastonite-enstatite-ferrosilite$_{55}$; Figure 5b and Table 3). Pyroxene in the groundmass has lower Na and higher Ca contents than the omphacitic inclusions and is dominantly diopside in composition (Figure 5b; $jadeite_{25}$wollastonite-enstatite-ferrosilite$_{75}$).

Amphibole analyses are normalized to 23 oxygens and classified using the scheme of *Leake et al.* [1997]. Amphibole shows a wide spectrum of compositions across the four samples with some variation associated with textural setting (Figure 5c and Tables 3 and 4). In eclogite sample AT2, glaucophane has a similar composition (Na_B: 1.94 pfu; Al^{VI}: 1.82 pfu) irrespective of textural setting (i.e., as inclusions in garnet and in the groundmass). In addition to the relicts of glaucophane in the groundmass amphibole, which is dominantly actinolite (Si: 7.97 pfu; Ca: 1.71 pfu; Al^{VI}: 0.25 pfu), small patches of ferroan hornblende (Si: 6.45 pfu; Ca: 1.93 pfu; Al^{VI}: 0.27 pfu) are present. In lawsonite-blueschist samples 47302, PC3B, and 7936, the amphibole defining the foliation is dominantly glaucophane (Figure 5c; Na_B: 1.93–1.80 pfu; Al^{VI}: 1.76–1.28 pfu) with minor amounts of earlier formed magnesiohornblende (Si: 6.39–6.51 pfu; Ca: 1.76–1.50 pfu; Al^{VI}: 0.46–0.95 pfu) (Table 4). The grains of calcic-amphibole rimmed by glaucophane are actinolitic-hornblende and have higher Si and lower Ca contents than the magnesiohornblende component of the foliation defining amphibole

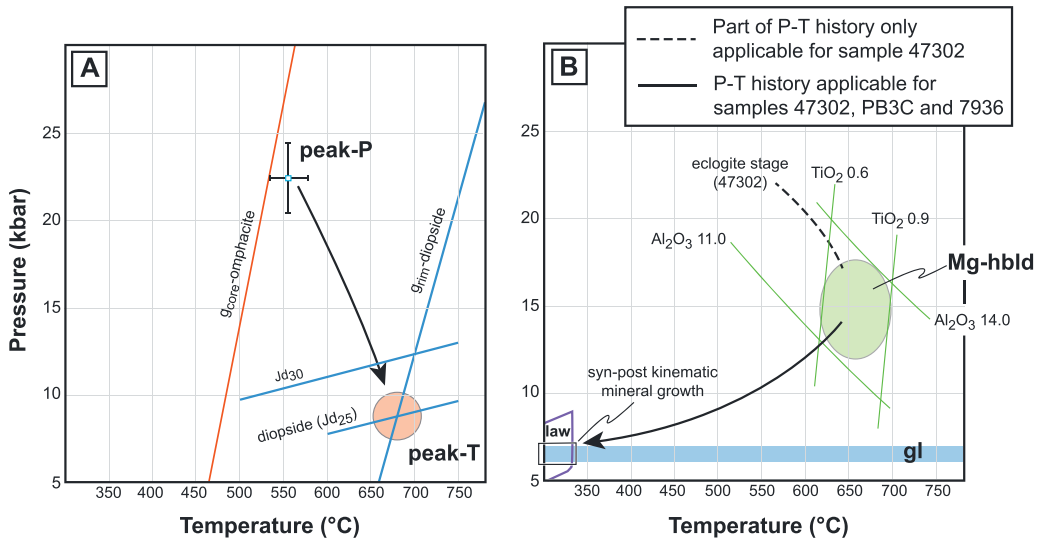

Figure 6. The results of thermobarometry and pressure-temperature paths compiled from these data. (a) *P-T* history for eclogite sample AT2. Orange ellipse is based on overlapping garnet-clinopyroxene thermometry [*Krogh-Ravna*, 2000] and jadeite in clinopyroxene barometry [*Essene and Fyfe*, 1967; *Holland*, 1980]. (b) *P-T* history for lawsonite-blueschist samples 7936, PB3C, and 47302. Green ellipse is based on isopleth-derived amphibole (magnesiohornblende-Mg-hbld) thermobarometry of *Ernst and Liu* [1998]. Low-pressure barometry (gl) is based on the Al_2O_3 content in sodic-amphibole barometer of *Maruyama et al.* [1986], the Na_{M4} versus Al^{IV} in glaucophane barometer of *Brown* [1977], and the presence of synkinematic lawsonite (law). Given the presence of garnet in sample 47302, an extended history from peak *P* eclogite conditions to amphibolite conditions is shown by a dashed black line.

(Si: 7.34 pfu; Ca: 1.47 pfu; Al^{VI}: 0.40 pfu). Owing to the low Ti contents of both magnesiohornblende and actinolitic-hornblende (<0.8% TiO_2), they are not assumed to be a primary igneous phase [cf. *Offler*, 1999].

Phengitic white mica formulae are normalized to 11 oxygens with total iron assumed to be Fe^{2+}. The silica content of white mica in all three samples of lawsonite-blueschist falls in the range of 3.64 and 3.28 pfu (Figure 5d and Table 4). In sample 7936, the inclusions of white mica encased in glaucophane have higher silica contents (3.69 pfu) than the phengite laths (3.28 pfu; Figure 5d) defining the foliation, as noted previously by *Offler* [1999]. Epidote formulae are normalized to 12.5 oxygens with total iron assumed to be Fe^{3+}. In all samples, epidote has a pistacite content ($Fe^{3+}/Fe^{3+} + Al + Mn$) of 0.20 to 0.22. Stoichiometric formulae of retrograde chlorite in eclogite sample AT2 are normalized to 28 oxygens with total iron assumed as Fe^{2+}. Compositionally, chlorite is an Fe-Mg solid solution where $X_{Mg}(X_{Mg}/X_{Fe} + X_{Mg} + X_{Mn}) = 0.48$. Feldspar in the groundmass of all samples has a restricted compositional range between $Ab_{0.96}$ and $Ab_{1.0}$ albite (Ab = Na/Ca).

Pressure-temperature (*P-T*) estimates of metamorphism for sample AT2 have been determined using optimal [*Powell and Holland*, 1994] and conventional thermobarometry techniques [*Holland*, 1980; *Krogh-Ravna*, 2000]. For optimal thermobarometry, end-member activities of $garnet_{core}$, omphacite, glaucophane, and epidote were calculated from the mineral compositional data using the AX program. Using the end-member activity data and pure end-members of H_2O, quartz and lawsonite, conditions of $P = 22.4 \pm 1.9$ kbar and $T = 556 \pm 23$°C were determined (Figure 6a). To verify this estimate, temperature conditions during the growth of $garnet_{cores}$ and omphacite were derived using the garnet-clinopyroxene thermometer of *Krogh-Ravna* [2000]. Temperature estimates between 465 and 545°C were determined using the mineral composition data over a range of pressure conditions (5–25 kbar). These results overlap with the *P-T* estimate determined using the optimal thermobarometry (Figure 6a). An approximate estimate of the pressure conditions during the growth of omphacite was also determined assuming an ideal pyroxene mixing model [*Essene and Fyfe*, 1967] and the experimentally determined albite = jadeite + quartz reaction [*Holland*, 1980]. However, given the absence of albite in the peak mineral assemblage, this estimate is regarded as a minimum approximation of the peak pressure conditions. Using a jadeite content of 0.3 mol proportion, pressures in the range of 9.6 to 13.0 kbar were calculated for the temperature range 500 to 750°C (Figure 6a).

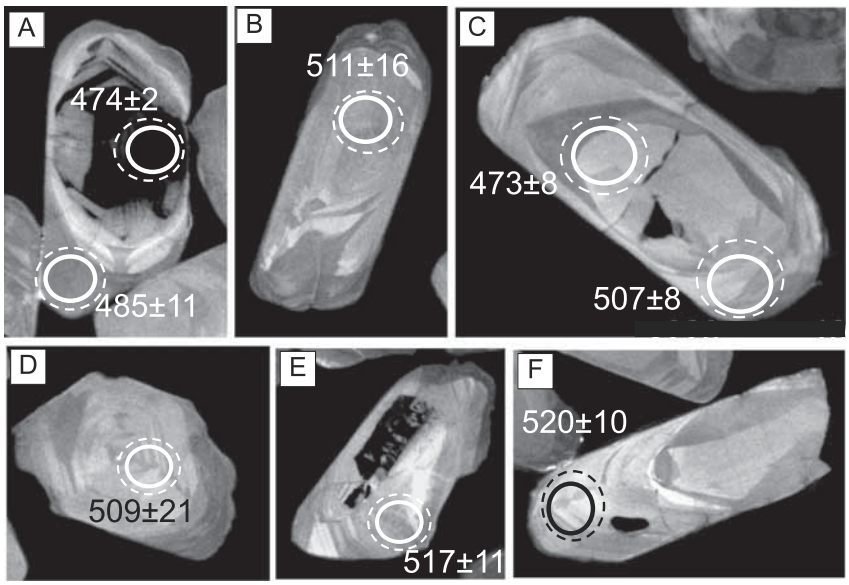

Figure 7. (a–f) Selected cathodoluminescence images of dated zircons. Numbers indicate $^{206}Pb/^{238}U$ ages ± Ma (1 sigma). Circles represent the location and size of the SHRIMP analysis (continuous line) and the laser ablation ICP-MS analysis (dotted line). The SHRIMP spot is 20 μm in diameter. Refer to text for details of age, trace element content, and textural relationships.

A tentative estimate of the *P-T* conditions of metamorphism during exhumation was calculated using the compositional data from texturally late mineral phases, namely, the garnet rims and diopside. Whereas an equilibrium relationship between these phases cannot be unequivocally proven, it is clear on textural grounds that these phases grew after the peak *P* $garnet_{core}$, omphacite, and glaucophane assemblage. Furthermore, as reaction textures and/or compositional zoning is lacking along the interfaces between the garnet and diopside, an equilibrium relationship between these phases can be reasonably inferred. The garnet-clinopyroxene thermometer of *Krogh-Ravna* [2000] approximates temperature conditions for the growth of the $garnet_{rims}$ and diopside to between 661 and 774°C ($P = 5–25$ kbar; Figure 6a). An approximate estimate of the pressure conditions during the growth of diopside was determined using the albite = jadeite + quartz reaction and a jadeite content of 0.25 mol proportion. Pressure conditions in the range of 7.8 to 8.4 kbar were calculated for the temperature range 600 to 800°C (Figure 6a). Given the presence of albite in the groundmass of the sample, we interpret this estimate to approximate the pressure conditions of metamorphism. Combining the results of the garnet-clinopyroxene thermometry and pyroxene barometry yields an estimate of 7.5–10.0 kbar and 650–700°C (Figure 6a).

A complex metamorphic paragenesis is inferred from the petrological relationships recorded in lawsonite-blueschist samples 7936, PB3C, and 47302. In order of relative timing, these stages of mineral growth are as follows: (i) growth of prograde garnet, as recorded by relicts in sample 47302, (ii) growth of phengite that is located as inclusions in the foliation defining amphibole, (ii) replacement of magnesiohornblende by glaucophane in the foliation defining amphibole, which was probably coeval with the growth of phengite, and (iv) the synkinematic to postkinematic growth of lawsonite. The presence of relict garnet in sample 47302 signifies that the dominant glaucophane-phengite assemblage formed during the retrograde part of the *P-T* history. Whereas the presence of garnet alone does not provide a necessary equilibrium assemblage for thermobarometry, the composition of these garnet fragments is comparable to the garnet cores in retrogressed eclogite sample AT2, both of which plot in the Group C eclogite field of *Coleman et al.* [1965] (Figure 5a) We therefore suggest that sample 47302 experienced an early eclogite stage of metamorphism (Figure 6b).

Using the Al_2O_3 (11.75–13.00 wt % oxide) and TiO_2 (0.66–0.76 wt % oxide) isopleth approach of *Ernst and Liu* [1998], the growth of early formed magnesiohornblende can be restricted to *P-T* conditions of 12.5–17.5 kbar and 620–700°C (Figure 6b). Pressure conditions associated with the subsequent growth of glaucophane (Na_B: 1.93–1.80 pfu; Al^{VI}: 1.76–1.28 pfu) can be approximated to between 6.5 and 7.5 kbar based on the empirical calibration of *Brown* [1977]. This estimate overlaps with those provided by the Al_2O_3 in sodic-amphibole barometer (8.00–11.28 wt % oxide) of *Maruyama et al.* [1986], which yields

AGU Tectonics

10.1002/2015TC003920

Table 6. SHRIMP U-Pb Analyses of Zircon Grains From Sample AT2[a]

Spot Name	% Initial ^{206}Pb	U (ppm)	Th (ppm)	$^{232}Th/^{236}$	Total $^{238}U/^{206}Pb$	% Error	Total $^{207}Pb/^{206}Pb$	% Error	$^{206}Pb/^{238}U$	±1 Sigma	$^{206}Pb/^{238}U$ Age (Ma)	±1 Sigma	CL Domain
AT2-24	0.40	6.9	0.03	0.004	15.60	2.70	0.05789	7.05	0.06386	0.00178	399	11	rim
AT2-33	5.70	1.3	0.01	0.008	13.99	5.37	0.10129	11.2	0.06741	0.00384	421	23	rim
AT2-11	2.73	0.5	0.01	0.027	13.59	8.83	0.07791	19.0	0.07158	0.00656	446	39	core sector
AT2-12	2.08	2.5	0.09	0.036	13.51	3.98	0.07282	11.3	0.07248	0.00303	451	18	rim
AT2-1	0.63	13.4	2.03	0.157	13.07	1.59	0.06159	4.11	0.07606	0.00126	**473**	**8**	core
AT2-15A	0.00	1281	75	0.060	13.12	0.65	0.05643	0.46	0.07624	0.00051	**474**	**3**	CL dark core
AT2-7	0.95	4.0	0.07	0.018	12.88	4.02	0.06437	8.00	0.07689	0.00318	**478**	**19**	rim
AT2-21	0.11	609	36.41	0.062	12.90	0.57	0.05763	0.66	0.07741	0.00045	**481**	**3**	CL dark core
AT2-30	1.95	5.6	0.15	0.027	12.62	5.48	0.07256	5.87	0.07769	0.00434	**482**	**26**	rim
AT2-16	0.11	2.8	0.16	0.059	12.82	3.48	0.05769	10.0	0.07789	0.00281	**484**	**17**	rim
AT2-14	2.33	1.1	0.02	0.017	12.54	5.60	0.07568	13.4	0.07790	0.00455	**484**	**27**	rim
AT2-15	0.24	6.9	0.09	0.013	12.77	2.23	0.05876	6.21	0.07813	0.00181	**485**	**11**	rim
AT2-9A	0.35	32.3	0.42	0.013	12.73	1.12	0.05970	2.64	0.07825	0.00090	**486**	**5**	core
AT2-20	0.41	2.4	0.07	0.028	12.71	3.86	0.06016	11.7	0.07838	0.00315	**486**	**19**	rim
AT2-2	4.06	1.3	0.08	0.062	12.23	5.27	0.08986	14.2	0.07844	0.00442	**487**	**26**	rim
AT2-18	0.00	2.1	0.06	0.028	12.86	4.12	0.04773	16.8	0.07865	0.00339	**488**	**20**	rim
AT2-8	0.34	25.1	0.03	0.001	12.51	1.22	0.05982	2.95	0.07964	0.00100	**494**	**6**	rim
AT2-3	0.00	1.0	0.02	0.024	12.60	5.91	0.05124	25.3	0.07994	0.00496	496	30	core sector
AT2-35	0.97	5.8	0.21	0.038	12.20	2.58	0.06517	6.70	0.08117	0.00218	*503*	*13*	rim
AT2-9	0.00	15.6	0.06	0.004	12.32	1.54	0.05447	4.07	0.08145	0.00129	*505*	*8*	rim
AT2-1A	0.11	23.8	0.32	0.014	12.20	1.58	0.05834	3.07	0.08189	0.00133	*507*	*8*	rim + core
AT2-17	0.86	1.4	0.05	0.035	12.10	8.08	0.06444	12.9	0.08195	0.00678	*508*	*40*	core sector
AT2-23	0.12	28.9	1.77	0.064	12.18	1.18	0.05844	2.83	0.08201	0.00099	*508*	*6*	rim
AT2-6	1.29	2.1	0.35	0.172	12.01	4.11	0.06794	12.2	0.08222	0.00354	*509*	*21*	core sector
AT2-10	0.00	4.5	0.05	0.012	12.14	5.30	0.05647	8.61	0.08245	0.00447	*511*	*27*	core
AT2-13	0.67	3.5	0.13	0.037	12.04	3.09	0.06299	7.75	0.08249	0.00264	*511*	*16*	core
AT2-32	0.79	1.2	0.04	0.035	11.92	5.88	0.06405	19.7	0.08321	0.00515	*515*	*31*	core sector
AT2-29	0.00	17.4	0.90	0.054	12.00	2.20	0.05577	3.69	0.08354	0.00188	*517*	*11*	rim
AT2-28	0.49	4.8	0.03	0.007	11.84	2.72	0.06170	6.77	0.08405	0.00236	*520*	*14*	rim
AT2-27	0.82	9.9	0.07	0.008	11.80	2.01	0.06439	5.05	0.08406	0.00176	*520*	*10*	rim
AT2-25	1.13	3.0	0.08	0.028	11.74	3.25	0.06696	9.23	0.08425	0.00286	*521*	*17*	rim
AT2-31	0.11	1.9	0.05	0.026	11.68	4.40	0.05886	14.3	0.08551	0.00393	*529*	*23*	rim
AT2-19	0.34	6.2	0.17	0.028	11.57	2.35	0.06085	8.30	0.08616	0.00213	*533*	*13*	rim
AT2-34	3.10	1.7	0.12	0.070	11.04	4.46	0.08360	9.54	0.08777	0.00410	*542*	*24*	rim
AT2-26	2.91	7.7	0.07	0.009	10.97	2.43	0.08211	5.71	0.08848	0.00228	*547*	*13*	rim
AT2-22	1.94	1.8	0.02	0.009	10.05	4.94	0.07580	14.2	0.09758	0.00510	600	30	rim

[a]Bold grouping represents the analyses that are used in the mean age calculations for the 480 ± 5 Ma population. Italic grouping represents the analyses that are used in the mean age calculations for the 514 ± 6 Ma population.

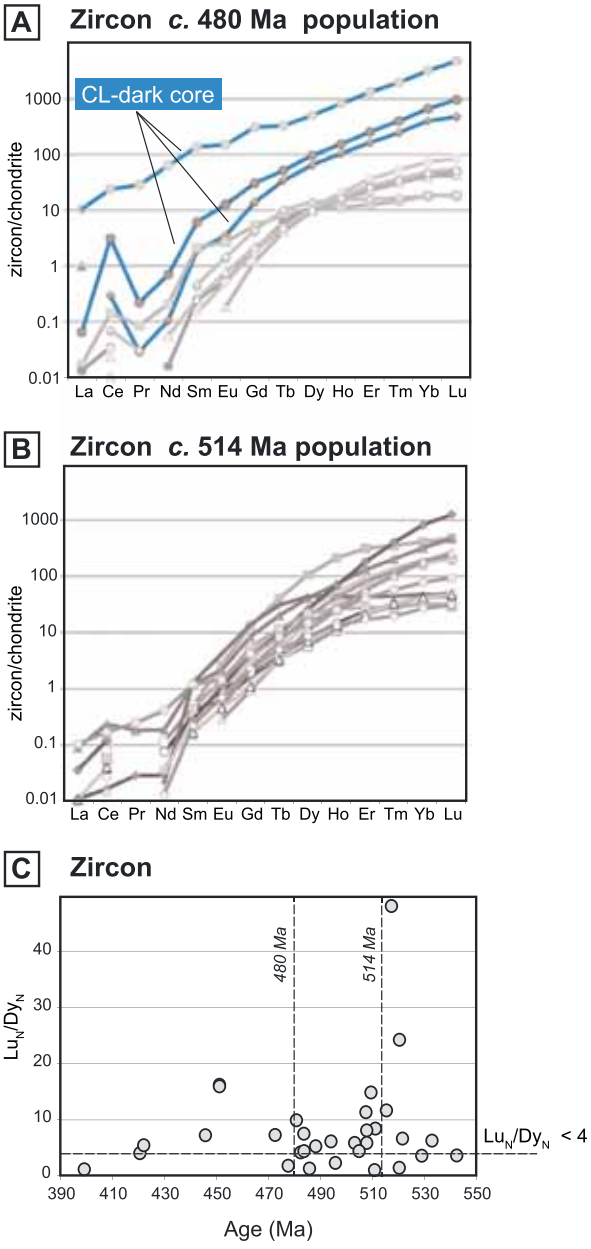

Figure 8. Summary plots of trace element data from zircon. (a) Zircon trace element patterns normalized to chondrite values [*McDonough and Sun*, 1995] for the ca. 480 Ma age population. Note that the CL dark cores have a steep, REE-rich pattern suggesting a magmatic origin (shown in blue). (b) Zircon trace element patterns normalized to chondrite values [*McDonough and Sun*, 1995] for the ca. 514 Ma age population. (c) Normalized La/Dy ratio in zircon versus zircon age; La/Dy ratios <4 are indicative of growth in the presence of garnet, which are common in both age populations.

estimates of between 6.0 and 7.0 kbar. These conditions are, however, regarded as a minimum estimate due to the lack of actinolite in the equilibrium assemblage. Accordingly, we suggest that ~7.5 kbar is a reasonable estimate of the pressure conditions of metamorphism during the growth of the glaucophane-phengite foliation assemblage. Given that lawsonite is both aligned and overgrows the glaucophane-phengite foliation, a synkinematic to postkinematic timing for mineral growth is assumed. Conditions for the stability of lawsonite are predicted thermodynamically by *Frey et al.* [1991] and provide a further constraint on the *P-T* evolution of the blueschist samples (Figure 6b). The composition of phengite cannot be used to quantify the pressure conditions of metamorphism due to the lack of a suitable buffering assemblage, yet the relative decrease in Si content from the early formed inclusions to the foliation defining phengite (Figure 5d) signifies a decrease in pressure during foliation development.

5.4. Geochronology

5.4.1. Zircon U-Pb Dating and Geochemistry

Zircon crystals in sample AT2 are generally weakly zoned with sector/fir tree-zoned cores and rims comprising weak oscillatory zoning (Figures 7a–7f). A few crystals have a CL dark core in which no zoning can be recognized. The zircons are poor in U (0.1–32.0 ppm) and very poor in Th (<1 ppm), with the exception of the CL dark cores (600–1280 ppm U and 36–75 ppm Th) (Table 6). Th/U is generally below 0.1 in all domains, with other trace elements varying significantly from crystal to crystal (Table 5). Ti concentrations are between 2 and 13 ppm, which corresponds to Ti-in-zircon temperatures between 610 and 770°C [*Ferry and Watson*, 2007].

Chondrite-normalized REE patterns (Figures 8a and 8b) vary between steep patterns with HREE enrichment up to 1000 times chondrite concentrations and moderate enrichment with HREE as low as 10 times chondrite. Negative Eu anomalies are minimal in all analyses (Eu/Eu^* 0.3–1.0). The Lu_N/Dy_N ratio (N = normalized to chondrite values), which reflects the steepness of the pattern, varies between 1 and 48 (Figure 8c).

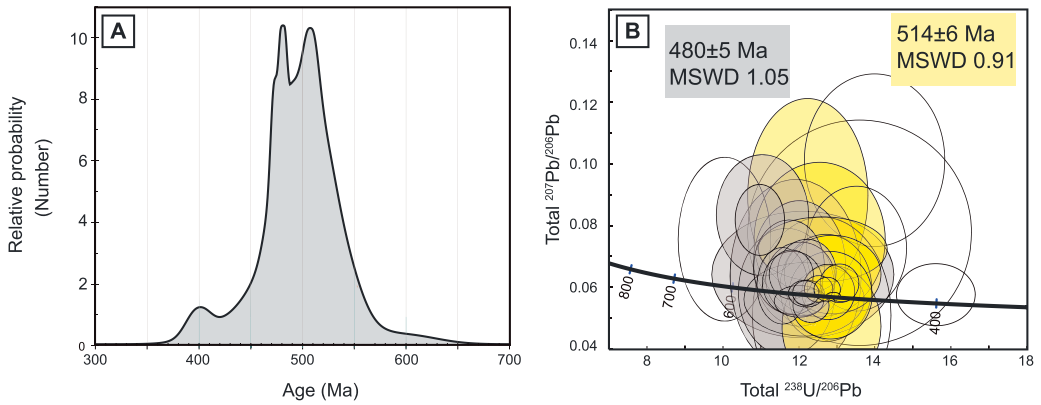

Figure 9. Summary plots of the U-Pb zircon data. (a) Probability density plot of $^{206}Pb/^{238}U$ ages showing the two groupings of age data. (b) Tera Wasserburg plot for U-Pb analyses uncorrected for common Pb. Average $^{206}Pb/^{238}U$ ages (±95% confidence level) are reported for the two main clusters (grey and yellow ellipses). Ellipses represent 2 sigma errors.

The very low U content makes U-Pb dating particularly challenging because of low Pb concentrations of radiogenic Pb and relatively high proportion of surface common Pb versus radiogenic Pb (f_{206} up to 5.7%; Table 6). The resulting ages are thus affected by variable errors (1–8% for 1 sigma). Calculated dates scatter between 400 and 600 Ma, with most analyses grouped in two clusters (Figure 9a). Data defining each cluster were used to calculate mean ages of 480 ± 5 Ma (mean square weighted deviation (MSWD) = 1.05) and 514 ± 6 Ma (MSWD = 0.91) (Figure 9b). The variation in age data does not correspond to zircon texture, as analyses from the weakly zoned zircon cores and rims fall into either age population and two of the analyzed CL dark cores are dated at 474 ± 2 and 473 ± 8 Ma (Figures 7a and 7c). In a few crystals where both core and rim were analyzed, the cores surprisingly returned younger dates than the rim (i.e., Figure 7c).

5.4.2. $^{40}Ar/^{39}Ar$ Thermochronology

The step-heating analysis of phengite defining the foliation in sample 7936 (Figure 3d) shows a general increase in age with increasing temperature steps (Figure 10a and Table 7). Significant discordance at the low- and high-temperature steps is probably due to the degassing of Ca-rich contaminant phases. A correlation between decreasing K/Ca ratios and increasing ages supports this inference (Figure 10a). A weighted mean age of 479 ± 1 Ma was calculated from four continuous steps showing low K/Ca ratios representing 31.7% of ^{39}Ar released (MSWD = 2.3; Figure 10a). The two-increment laser heating analyses reveal a bimodal distribution of age data with a general grouping between 480 and 490 Ma (n = 22; Figure 10b and Table 7). Compared to the furnace step-heating age data, a slightly older weighted mean age of 482 ± 1 Ma (n = 8; MSWD = 3.6) is calculated. This age is interpreted to represent the cooling of sample 7936 through the bulk closure temperature of argon diffusion in phengite (T_c ~ 350°C).

Phengite defining the foliation was also separated from sample PB3C for $^{40}Ar/^{39}Ar$ analysis. The age spectrum yielded from the step-heating analysis consists of discordant low- and high-temperature steps (Figure 10c and Table 7). Owing to the relatively consistent K/Ca ratios for each heating step, age discordance could be due to a number of factors ranging from slow cooling, variations in cooling ages between grains of different sizes, or recoil artifacts causing Ar and/or K loss. From the age spectrum, a weighted mean age of 478 ± 1 Ma was calculated from two continuous steps representing 63.3% of ^{39}Ar released. Two-increment heating experiments were carried out on single grains from the same sample to verify this age as the timing of closure for argon diffusion in phengite. A probability plot compiled from 18 analyses shows a slight bimodal distribution in the age data. From these data, a weight mean age of 482 ± 2 Ma (n = 9; MSWD = 6.1) is calculated (Figure 10d and Table 7), which is interpreted to represent the cooling of sample PB3C through ~350°C.

6. Discussion

6.1. Relevance of Zircon U-Pb and Geochemistry

To determine if the calculated ages represent protolith crystallization or metamorphism of sample AT2, we examined the relationship between zircon texture, U-Pb isotope, and chemical composition. The textural

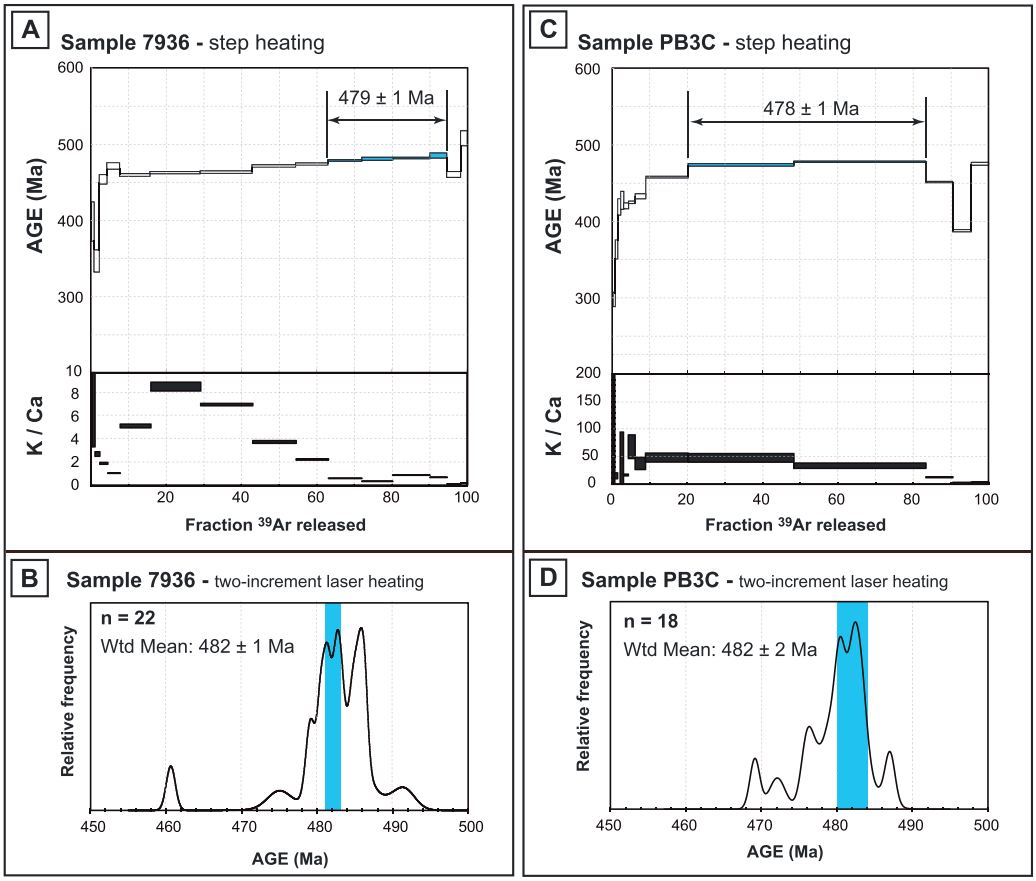

Figure 10. Summary plots of $^{49}Ar/^{39}Ar$ isotopic data. (a) Step-heating analysis of sample 7936. Steps used to calculate the mean age are shaded in blue. (b) Cumulative frequency plot of total data from the two-increment single-grain laser fusion analysis for sample 7936. Blue shading shows the range determined by the weighted mean age calculation. (c) Step-heating analysis of sample PB3C. Steps used to calculate the mean age are shaded in blue. (d) Cumulative frequency plot of total data from the two-increment single-grain laser fusion analysis for sample PB3C. Blue shading shows the range determined by the weighted mean age calculation.

relationship between dark CL cores and light CL rims (Figure 7a) indicates two stages of growth. To some degree, the geochemical data support this interpretation as the dark CL cores can have a distinct magmatic composition (rich in U and Th, high HREE content, and a steep pattern; Figure 8a) that is in contrast with metamorphic zircon [*Rubatto*, 2002]. The age data, however, confound this interpretation, because (i) cores can have younger ages than the rims (Figures 7a and 7c) and (ii) analyses defining the older age grouping are not necessarily only from the dark CL cores (Figures 7e and 7f). This disconnection between zircon texture, trace element composition, and U-Pb age supports the concept that trace element content is more resistant to resetting than isotopic U-Pb [*Cherniak et al*., 1997; *Cherniak and Watson*, 2001]. We propose that in our sample the U, Th, and HREE compositions of the CL dark cores reflect magmatic growth conditions (of unknown age), yet their U-Pb composition was later reset. This scenario has been documented in eclogites of the Dabie-Sulu terrain, where abundant inherited cores frequently preserve distinct chemistry but U-Pb ages were reset during metamorphism [e.g., *Xia et al*., 2009].

The lack of systematic correlation between texture, HREE enrichment, and Ti content is taken as reflecting zircon growth in an evolving equilibrium volume during metamorphism. It is however of significance that zircon grains defining both 514 ± 6 and 480 ± 5 age group show flat HREE signatures ($LuN/DyN < 4$, Figure 8c). Notably, flat HREE patterns have never been observed in magmatic zircons and are typical of zircons that have grown in a garnet-rich assemblage [*Rubatto*, 2002; *Hermann and Rubatto*, 2003]. We therefore suggest that zircon growth/recrystallization in sample AT2 took place at both 514 ± 6 and 480 ± 5 in an equilibrium

Table 7. Step-Heating and Laser Fusion $^{40}Ar/^{39}Ar$ Analyses of Phengite From Samples PB3C and 7936

				^{40}Ar	±	^{39}Ar	±	^{38}Ar	±	^{37}Ar	±	^{36}Ar	±							
		Step No.	Cum.% ^{39}Ar	($\times10^{-13}$ mol)		($\times10^{-14}$ mol)		($\times10^{-16}$ mol)		($\times10^{-16}$ mol)		($\times10^{-16}$ mol)		Ca/K (Ma)	±	% $^{40}Ar^*$	$^{40}Ar^*/^{39}Ar$	±	Age	±
Step-Heating Analysis: Sample PB3C																				
	J-Value		0.015093	0.000028	0.18															
Temp (°C)	700		0.52	0.1032	0.0002	0.0766	0.0003	0.0004	0.0139	0.0225	0.0861	0.0424	0.0105	0.0051	0.0197	87.9	11.83	0.41	296.3	9.4
	750		1.20	0.1572	0.0002	0.0996	0.0005	0.0004	0.0199	0.4298	0.1749	0.0346	0.0189	0.0755	0.0307	93.5	14.75	0.57	362.6	12.6
	780		1.90	0.1776	0.0002	0.1015	0.0005	0.0004	0.0171	0.0043	0.0007	0.0066	0.0169	0.0007	0.0001	98.9	17.30	0.50	418.6	10.8
	810		2.79	0.2340	0.0003	0.1304	0.0005	0.0004	0.0272	0.1897	0.2633	0.0103	0.0239	0.0254	0.0353	98.7	17.70	0.55	427.2	11.7
	840		4.02	0.3193	0.0005	0.1811	0.0007	0.0004	0.0144	0.7027	0.0698	0.0163	0.0099	0.0679	0.0068	98.5	17.36	0.18	419.9	3.9
	870		5.82	0.4625	0.0006	0.2630	0.0011	0.0004	0.0369	0.2243	0.0725	0.0003	0.0004	0.0149	0.0048	100.0	17.58	0.08	424.6	1.6
	900		8.66	0.7563	0.0009	0.4169	0.0011	0.0004	0.0214	0.6609	0.2070	0.0276	0.0202	0.0277	0.0087	98.9	17.95	0.15	432.4	3.3
	950		19.94	3.1775	0.0039	1.6524	0.0023	0.1060	0.0505	2.0141	0.3494	0.0462	0.0212	0.0213	0.0037	99.6	19.15	0.05	458.0	1.1
	1000		48.12	8.2528	0.0085	4.1302	0.0057	0.0004	0.1387	5.0870	0.8653	0.1018	0.1003	0.0216	0.0037	99.6	19.91	0.08	474.0	1.7
	1100		83.24	10.3773	0.0105	5.1466	0.0071	0.3119	0.1566	9.2018	1.3948	0.0921	0.0149	0.0313	0.0047	99.7	20.11	0.04	478.2	0.7
	1200		90.41	1.9875	0.0024	1.0514	0.0007	0.0237	0.0285	5.7036	0.3362	0.0255	0.0112	0.0949	0.0056	99.6	18.83	0.04	451.3	0.9
	1350		95.40	1.1882	0.0013	0.7315	0.0010	0.0245	0.0229	52.6238	0.2007	0.0952	0.0131	1.2590	0.0051	97.6	15.86	0.06	387.2	1.3
	1450		100.00	1.3924	0.0020	0.6737	0.0016	0.2369	0.0879	29.3233	1.2412	0.1576	0.0156	0.7617	0.0323	96.7	19.98	0.09	475.4	1.8
Step-Heating Analysis: Sample 7936																				
	J-Value		0.015097	0.000028	0.19															
Temp (°C)	700		0.73	0.1047	0.0002	0.0538	0.0003	0.0004	0.0168	0.3311	0.2088	0.0569	0.0215	0.1078	0.0680	84.0	16.36	1.19	398.2	25.9
	750		2.10	0.1961	0.0002	0.1013	0.0004	0.0664	0.0175	2.0798	0.1521	0.1835	0.0220	0.3594	0.0263	72.3	14.00	0.65	346.0	14.5
	800		4.14	0.3014	0.0004	0.1509	0.0005	0.0004	0.0068	4.4158	0.1749	0.0543	0.0148	0.5121	0.0204	94.7	18.91	0.30	453.1	6.3
	850		7.46	0.4936	0.0005	0.2452	0.0010	0.0004	0.0171	13.0260	0.1390	0.0327	0.0146	0.9298	0.0107	98.0	19.74	0.20	470.6	4.1
	900		15.60	1.1977	0.0014	0.6011	0.0008	0.0022	0.0322	6.5072	0.1994	0.1434	0.0143	0.1894	0.0058	96.5	19.22	0.08	459.6	1.7
	930		28.94	1.9401	0.0022	0.9852	0.0013	0.0004	0.0339	6.4060	0.2809	0.1081	0.0197	0.1138	0.0050	98.4	19.37	0.07	462.8	1.4
	950		42.75	2.0101	0.0021	1.0192	0.0013	0.0387	0.0359	8.1014	0.1110	0.1099	0.0225	0.1391	0.0019	98.4	19.40	0.07	463.5	1.5
	970		54.34	1.7020	0.0020	0.8558	0.0013	0.0506	0.0327	12.6623	0.3793	0.0499	0.0175	0.2589	0.0078	99.1	19.72	0.07	470.1	1.5
	990		62.96	1.2823	0.0014	0.6367	0.0015	0.0030	0.0260	15.8718	0.4333	0.0618	0.0098	0.4362	0.0120	98.6	19.85	0.07	472.9	1.5
	1020		71.99	1.3827	0.0016	0.6670	0.0007	0.0341	0.0286	61.7859	0.3309	0.1496	0.0082	1.6211	0.0089	96.8	20.07	0.05	477.4	1.0
	1050		80.19	1.2538	0.0014	0.6055	0.0009	0.0632	0.0170	98.6344	0.2376	0.1089	0.0163	2.8509	0.0080	97.4	20.18	0.09	479.7	1.8
	1100		90.07	1.4954	0.0017	0.7301	0.0007	0.0096	0.0402	46.5565	0.2420	0.0644	0.0101	1.1160	0.0059	98.7	20.22	0.05	480.7	1.1
	1150		94.62	0.6897	0.0008	0.3359	0.0010	0.0004	0.0175	27.0408	0.2493	0.0175	0.0172	1.4088	0.0136	99.2	20.38	0.16	483.9	3.4
	1350		98.23	0.5449	0.0006	0.2664	0.0011	0.0380	0.0169	143.6494	0.7920	0.1115	0.0155	9.4359	0.0640	94.0	19.22	0.19	459.6	4.0
	1450		100.00	0.2996	0.0004	0.1306	0.0006	0.0004	0.0087	39.2115	0.1583	0.0640	0.0200	5.2532	0.0309	93.7	21.49	0.46	506.9	9.5
Single-Grain Laser Analysis: Sample PB3C																				
	J-Value	0.015093	0.000028																	
Sample	3C-1	1	5.8	1.0605	0.0014	0.5394	0.0006	0.0002	0.0176	4.195	0.183	0.0571	0.0030	0.136	0.006	98.4	19.35	0.04	462.2	0.8
ID		2	7.4	0.2956	0.0004	0.1499	0.0002	0.0020	0.0076	4.102	0.241	0.0136	0.0010	0.479	0.028	98.6	19.46	0.04	464.5	0.9
	3C-2	1	10.0	0.4579	0.0007	0.2403	0.0004	0.0041	0.0066	32.893	0.495	0.0258	0.0023	2.396	0.036	98.3	18.74	0.05	449.3	1.1
	3C-3	1	13.7	0.6867	0.0009	0.3442	0.0006	0.0002	0.0112	0.553	0.059	0.0155	0.0025	0.028	0.003	99.3	19.82	0.05	472.1	1.1
		2	19.0	0.9923	0.0014	0.4919	0.0008	0.0002	0.0138	4.152	0.228	0.0167	0.0014	0.148	0.008	99.5	20.07	0.04	477.4	0.9
	3C-4	1	25.7	1.2402	0.0015	0.6166	0.0007	0.0002	0.0194	1.162	0.216	0.0232	0.0025	0.033	0.006	99.4	20.00	0.04	476.0	0.7
		2	31.3	1.0564	0.0013	0.5228	0.0006	0.0002	0.0141	1.390	0.179	0.0104	0.0019	0.047	0.006	99.7	20.15	0.04	479.0	0.7
		3	35.7	0.8223	0.0020	0.4065	0.0005	0.0002	0.0153	1.523	0.172	0.0008	0.0044	0.066	0.007	100.0	20.22	0.06	480.6	1.3
	3C-5	1	39.2	0.6635	0.0009	0.3256	0.0002	0.0002	0.0092	0.591	0.044	0.0188	0.0009	0.032	0.002	99.2	20.21	0.03	480.2	0.6
		2	45.0	1.0975	0.0014	0.5380	0.0004	0.0002	0.0155	1.591	0.124	0.0112	0.0022	0.052	0.004	99.7	20.34	0.03	482.9	0.7
	3C-6	1	46.0	0.1866	0.0003	0.0947	0.0005	0.0002	0.0032	1.154	0.130	0.0062	0.0010	0.213	0.024	99.0	19.52	0.11	465.9	2.2
		2	48.1	0.3913	0.0005	0.1896	0.0002	0.0002	0.0070	0.501	0.097	0.0177	0.0017	0.046	0.009	98.7	20.36	0.04	483.4	0.9
	3C-7	1	53.7	1.0696	0.0013	0.5237	0.0007	0.0002	0.0144	1.153	0.100	0.0308	0.0023	0.039	0.003	99.1	20.25	0.04	481.1	0.8
		2	56.9	0.6041	0.0008	0.2968	0.0007	0.0002	0.0078	0.732	0.066	0.0093	0.0021	0.043	0.004	99.5	20.26	0.06	481.4	1.2
		3	58.1	0.2326	0.0003	0.1138	0.0004	0.0002	0.0049	0.210	0.208	0.0007	0.0018	0.032	0.032	99.9	20.42	0.09	484.7	1.8

AGU Tectonics

10.1002/2015TC003920

Table 7. (continued)

				^{40}Ar	±	^{39}Ar	±	^{38}Ar	±	^{37}Ar	±	^{36}Ar	±						
		Step No.	Cum.% ^{39}Ar	($\times10^{-13}$ mol)		($\times10^{-14}$ mol)		($\times10^{-16}$ mol)		($\times10^{-16}$ mol)		($\times10^{-16}$ mol)		Ca/K (Ma)	±	$\%^{40}Ar^{*}$	$^{40}Ar^{*}/^{39}Ar$	±	Age	±
	3C-8	1	62.7	0.8610	0.0012	0.4223	0.0005	0.0002	0.0113	0.966	0.143	0.0244	0.0016	0.040	0.006	99.2	20.22	0.04	480.4	0.9
		2	65.9	0.6143	0.0008	0.2987	0.0003	0.0002	0.0079	1.443	0.082	0.0224	0.0024	0.085	0.005	98.9	20.34	0.04	483.1	0.9
	3C-9	1	71.6	1.0535	0.0013	0.5326	0.0004	0.0002	0.0157	3.028	0.187	0.0189	0.0015	0.099	0.006	99.5	19.68	0.03	469.1	0.7
		2	73.9	0.4267	0.0008	0.2127	0.0006	0.0002	0.0084	2.652	0.063	0.0100	0.0016	0.218	0.005	99.3	19.92	0.07	474.2	1.4
	3C-10	1	76.6	0.5115	0.0006	0.2471	0.0005	0.0002	0.0080	0.784	0.078	0.0522	0.0025	0.056	0.006	97.0	20.08	0.06	477.5	1.2
		2	82.0	1.0169	0.0013	0.4982	0.0002	0.0002	0.0136	1.204	0.133	0.0191	0.0013	0.042	0.005	99.4	20.30	0.03	482.1	0.6
	3C-11	1	86.5	0.8426	0.0011	0.4167	0.0009	0.0002	0.0115	1.336	0.125	0.0248	0.0028	0.056	0.005	99.1	20.04	0.05	476.8	1.1
		2	92.1	1.0779	0.0014	0.5234	0.0004	0.0002	0.0183	2.408	0.269	0.0108	0.0010	0.081	0.009	99.7	20.53	0.03	487.0	0.7
	3C-12	1	94.0	0.3328	0.0005	0.1754	0.0004	0.0002	0.0055	0.822	0.065	0.0271	0.0017	0.082	0.006	97.6	18.52	0.06	444.7	1.3
		2	100.0	1.1155	0.0015	0.5581	0.0006	0.0002	0.0158	9.830	0.230	0.0275	0.0016	0.308	0.007	99.3	19.84	0.03	472.6	0.7
									Single-Grain Laser Analysis: Sample 7936											
	J-Value	0.021740	0.000034																	
Sample	7936-1a	1	56.1	0.7049	0.0010	0.4921	0.0006	0.0002	0.0156	0.9767	0.1124	0.0367	0.0041	0.0347	0.0040	98.5	14.10	0.04	482.5	1.1
ID		2	100.0	0.5202	0.0006	0.3850	0.0005	0.0002	0.0126	0.9956	0.1363	0.0172	0.0042	0.0453	0.0062	99.0	13.38	0.04	460.6	1.2
	7936-2a	1	90.4	0.5563	0.0007	0.3867	0.0004	0.0002	0.0118	1.6941	0.1749	0.0270	0.0044	0.0767	0.0079	98.6	14.18	0.04	484.7	1.2
		2	100.0	0.0605	0.0001	0.0412	0.0003	0.0001	0.0044	2.0764	0.1595	0.0089	0.0043	0.8830	0.0681	95.6	14.06	0.33	481.2	9.8
	7936-3a	1	40.8	0.3504	0.0004	0.2404	0.0002	0.0002	0.0073	0.2424	0.1937	0.0375	0.0025	0.0176	0.0141	96.8	14.12	0.04	482.9	1.1
		2	100.0	0.5050	0.0007	0.3489	0.0006	0.0002	0.0105	1.1749	0.1805	0.0304	0.0016	0.0589	0.0091	98.2	14.22	0.03	485.9	1.0
	7936-4a	1	78.2	0.4268	0.0005	0.2979	0.0006	0.0002	0.0095	2.7795	0.1036	0.0327	0.0036	0.1633	0.0061	97.7	14.00	0.05	479.4	1.4
		2	100.0	0.1247	0.0001	0.0828	0.0003	0.0005	0.0047	10.4873	0.1574	0.0336	0.0025	2.2155	0.0340	92.0	13.85	0.10	475.0	3.1
	7936-5a	1	68.4	0.6838	0.0008	0.4738	0.0002	0.0133	0.0136	6.8213	0.2035	0.0361	0.0043	0.2519	0.0075	98.4	14.20	0.03	485.5	1.0
		2	100.0	0.3769	0.0005	0.2186	0.0004	0.0474	0.0080	3.7782	0.3452	0.2234	0.0049	0.3025	0.0276	82.5	14.23	0.07	486.2	2.2
	7936-6a	1	88.6	0.6450	0.0008	0.4521	0.0005	0.0149	0.0128	2.7781	0.1932	0.0312	0.0032	0.1075	0.0075	98.6	14.06	0.03	481.3	0.9
		2	100.0	0.0821	0.0001	0.0581	0.0001	0.0002	0.0030	0.9171	0.1716	0.0002	0.0001	0.2764	0.0517	99.9	14.13	0.04	483.3	1.3
	7936-7a	1	93.2	0.9335	0.0011	0.6394	0.0003	0.0253	0.0165	2.3868	0.3349	0.0795	0.0047	0.0653	0.0092	97.5	14.23	0.03	486.3	0.9
		2	100.0	0.0681	0.0001	0.0467	0.0001	0.0019	0.0023	0.8478	0.1772	0.0075	0.0023	0.3180	0.0665	96.7	14.11	0.16	482.7	4.7
	7936-8a	1	80.5	0.2702	0.0003	0.1893	0.0004	0.0120	0.0057	1.0182	0.1935	0.0133	0.0024	0.0941	0.0179	98.5	14.07	0.05	481.5	1.5
		2	100.0	0.0727	0.0002	0.0459	0.0002	0.0057	0.0020	1.8389	0.2053	0.0241	0.0023	0.7012	0.0783	90.2	14.28	0.17	487.7	5.0
	7936-9a	1	49.5	0.6327	0.0011	0.4479	0.0009	0.0002	0.0123	1.3164	0.1708	0.0100	0.0034	0.0514	0.0067	99.5	14.06	0.04	481.1	1.3
		2	100.0	0.6410	0.0008	0.4564	0.0004	0.0028	0.0139	5.0553	0.2285	0.0014	0.0029	0.1938	0.0088	99.9	14.04	0.03	480.4	0.9
	7936-10a	1	83.2	0.5432	0.0007	0.3670	0.0002	0.0226	0.0130	5.2006	0.1760	0.0774	0.0037	0.2480	0.0084	95.8	14.18	0.04	484.7	1.1
		2	100.0	0.1089	0.0002	0.0740	0.0002	0.0015	0.0066	6.0525	0.2179	0.0076	0.0021	1.4306	0.0516	97.9	14.41	0.09	491.5	2.8
	7936-11a	1	72.1	0.9565	0.0013	0.6642	0.0006	0.0466	0.0198	4.8135	0.2720	0.0926	0.0069	0.1268	0.0072	97.1	13.99	0.04	-	-
		2	100.0	0.3812	0.0005	0.2573	0.0005	0.0106	0.0086	4.0243	0.2307	0.0615	0.0033	0.2737	0.0157	95.2	14.11	0.05	482.7	1.5

Tectonics

10.1002/2015TC003920

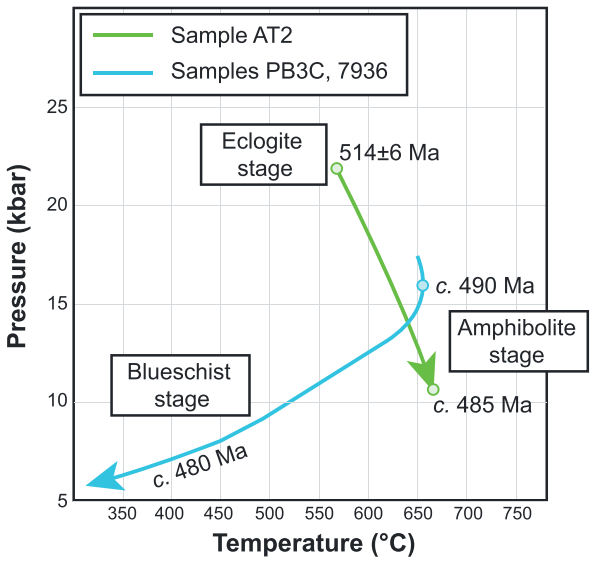

Figure 11. Summary of pressure-temperature-time histories for eclogite sample AT2 (green) and lawsonite-blueschist samples PB3C and 7936 (blue). Note that the amphibolite stage represents the late part of the preserved *P-T* evolution of sample AT2, and the early part of samples PB3C and 7936. The relevance of this observation is discussed in the text.

volume containing garnet. Accordingly, sample AT2 must have been at blueschist to eclogite facies conditions by at least 514 ± 6 Ma, and the U-Pb system of some zircon domains was significantly reset at 480 ± 5 Ma. The possible cause of this resetting is discussed below.

6.2. History of High-Pressure Rocks in the Peel-Manning Ophiolite

Prior to their incorporation into the Peel-Manning Ophiolite, high-pressure metamorphic rocks formed under eclogite to blueschist facies conditions during the Cambrian. Based on our U-Pb zircon data, the timing of eclogite facies metamorphism recorded by eclogite sample AT2 can be revised to 514 ± 6 Ma (Figure 11) [cf. *Fanning et al.*, 2002]. As subduction is a continuous process, we interpret this age to reflect the timing that eclogite sample AT2 was detached from the downgoing slab; otherwise, continued subduction would have resulted in further burial and development of a higher-*P* mineral assemblage. Exhumation and underplating of sample AT2 were probably facilitated by return flow in the subduction channel [*Cloos*, 1982; *Gerya et al.*, 2002]. Recrystallization of eclogite sample AT2 at amphibolite facies conditions (7.5–10.0 kbar and 650–700°C) was responsible for the growth of the garnet$_{rims}$-diopside assemblage (Figure 11). Where an unequivocal link between the growth of this mineral assemblage and the zircon U-Pb isotope data cannot be made, we favor an interpretation where metamorphic recrystallization at amphibolite facies conditions was coeval with the resetting of U-Pb systematics at 480 ± 5 Ma (Figure 11). This interpretation is supported by the zircon trace element data, which indicate zircon growth/recrystallization at this time was in the presence of garnet (i.e., $Lu_N/Dy_N < 4$; Figure 8c).

The metamorphic histories of all three lawsonite-blueschist samples are defined by an early to middle amphibolite stage (*P-T* conditions of 12.5–17.5 kbar and 620–700°C) followed by a blueschist stage (*P-T* conditions of ~7.5 kbar and 300–350°C; Figure 11). Given that the amphibole grains defining the foliation comprise early formed magnesiohornblende overprinted by glaucophane and that phengite and lawsonite are aligned with the same foliation, we interpret the amphibolite and blueschist stages as synkinematic. There is also evidence that some of the lawsonite-blueschist samples probably attained eclogite facies conditions prior to the amphibolite stage, which comes from the identified relics of eclogitic garnet in sample 47302. Our $^{40}Ar/^{39}Ar$ data place timing constraints on the *P-T* history of the lawsonite-blueschists by limiting the time that the samples cooled through the closure temperature of argon diffusion in white mica (T_c ~ 350°C). Given that our estimate of *T* for the blueschist (300–350°) stage overlaps with the closure temperature of argon diffusion in white mica, the age data provide an absolute timing constraint on the synkinematic-postkinematic history of the lawsonite-blueschist samples. Accordingly, we suggest that the lawsonite-glaucophane-phengite assemblage probably formed between 485 and 480 Ma. Furthermore, given the synkinematic relationship between the minerals grown during the amphibolite and blueschist stages, we suggest a continuous *P-T* history as opposed to two separate metamorphic events separated by a significant interval in time. Accordingly, 490–480 Ma is probably a reasonable approximation for the timing of amphibolite-blueschist metamorphism of the lawsonite-blueschist samples (Figure 11).

6.3. Geodynamic Implications of Pressure-Temperature-Time Histories

Previously available geochronological data from an eclogite block at Attunga are used in support of a multiple-subduction-zone model for the early Cambrian evolution of the Tasmanides [*Glen*, 2013]. This model

is largely based on (i) a 536 + 18 Ma U-Pb zircon age for eclogite facies metamorphism [*Fanning et al*., 2002], which, as argued by *Glen* [2013], was approximately 10–20 million years older than the postulated onset of the Delamerian Orogeny (ca. 520 Ma) and (ii) the considerable distance (approximately 1000 km) between the Delamerian margin (i.e., the Koonenberry Belt) and the Peel-Manning Fault System (Figure 1b). Accordingly, *Glen* [2013] prefers a model where the eclogite blocks located in the Peel-Manning Fault System formed in an older intraoceanic subduction zone (530–520 Ma) that was located to the east of the Australian continental margin. Given that the main line of argument is based on the age of subduction zone metamorphism in the Peel-Manning Fault System, we refute the reconstruction of *Glen* [2013], as our new U-Pb zircon data revise the timing of eclogite formation from 536 + 18 Ma to 514 ± 6 Ma. As our revised timing of subduction zone metamorphism better overlaps with the early stages of the Delamerian Orogeny, we cannot dismiss the possibility that a genetic link exists between the formation and exhumation of sample AT2 and subduction responsible for the Delamerian Orogeny. This conclusion, however, poses a significant question, namely, how did high-pressure rocks formed during the Cambrian Delamerian Orogeny become translated and exposed in the Devonian-Carboniferous New England Orogen? We discuss this in the following section.

Amphibolite facies metamorphism of high-pressure rocks in the Peel-Manning Fault System at ca. 485 Ma overlaps with a major geodynamic event in the Tasmanides, namely, the transition between the Delamerian and Lachlan orogenies. East directed rollback of the subduction zone is the preferred mechanism for the relocation of subduction, which may have been triggered by a decrease in the negative buoyancy force of the subducting slab due to it reaching the 650 km mantle discontinuity [*Foden et al*., 2006]. Subduction zone rollback has been shown to inject new mantle material into the mantle wedge [*Kincaid and Griffiths*, 2003], a process that we argue is recorded by the high-pressure metamorphic rocks studied here. For in the high-pressure metamorphic rocks underplated prior to rollback heating (i.e., sample AT2), the high-temperature amphibolite stage occurs relatively late in the *P-T* evolution and overprints an earlier formed eclogite facies mineral assemblage (Figure 11). For samples exhumed and/or underplated during rollback, the amphibolite stage is recorded in the early to middle stages of the *P-T* evolution (i.e., samples PB3C and 7936; Figure 11). After rollback, cooling of the subduction zone would follow the establishment of a stable subduction hinge, as the cold slab refrigerates [*Peacock*, 1996] the recently injected hot mantle material. In samples containing hydrous mineral phases and/or receiving a significant influx of fluid from an external source, metamorphic recrystallization during exhumation and cooling would produce a pervasive blueschist overprint (i.e., samples PB3C and 7936). In samples comprising anhydrous eclogite mineral assemblages, fluid availability would be limited to external sources, and the effects of metamorphism at blueschist facies conditions would probably be limited (i.e., sample AT2).

6.4. Postulated History of the Peel-Manning Ophiolite and High-Pressure Rocks

The geochemical signatures of ultramafic to mafic rocks of the Peel-Manning Ophiolite indicate derivation from a highly refractory mantle source, which is consistent with formation in an extended intraoceanic arc setting [*Cross*, 1983; *Aitchison et al*., 1994]. Age control on ophiolite formation comes from blocks of plagiogranite entrained in the serpentinite matrix mélange zones, which record U-Pb zircon ages of ca. 530 Ma [*Aitchison et al*., 1992; *Aitchison and Ireland*, 1995]. Given these data, we propose a model where the Peel-Manning Ophiolite formed in an intraoceanic suprasubduction setting during the Early Cambrian history of the Delamerian Orogeny (Figure 12a). However, to explain the continental protolith of some of the high-pressure rocks (e.g. sample 7936), we propose that the subduction zone formed close to the continental margin and experienced an immediate eastward retreat into an intraoceanic setting. Hinge retreat extended the overriding plate and resulted in the rifting of continental ribbons from the leading edge of the continent; parts of which were later detached by tectonic erosion and subsequently subducted (Figure 12a). Our model supports the work of *Crawford et al.* [1997], who proposed that Cambrian-aged calc-alkaline magmatism in the Koonenberry Belt formed by the partial melting of subcontinental lithospheric mantle in an immature continental rift setting (as opposed to an Andean-type continental arc as proposed by *Greenfield et al*. [2011] and *Glen* [2013]). Cambrian-aged, island arc-derived volcaniclastic rocks in the Tamworth Belt, along with the mafic igneous complexes in the Lachlan Orogen [*Crawford et al*., 1984] may have also formed in this intraoceanic setting. Once subduction was established, it is likely that the exhumation of high-pressure metamorphic rocks took place by returned flow in the subduction channel [*Gerya et al*., 2002], which resulted in their accumulation below the ophiolite (Figure 12a). Widespread crustal shortening heralded the end of the Delamerian Orogenic stage, which may have been driven by the arrival of an asperity on the downgoing

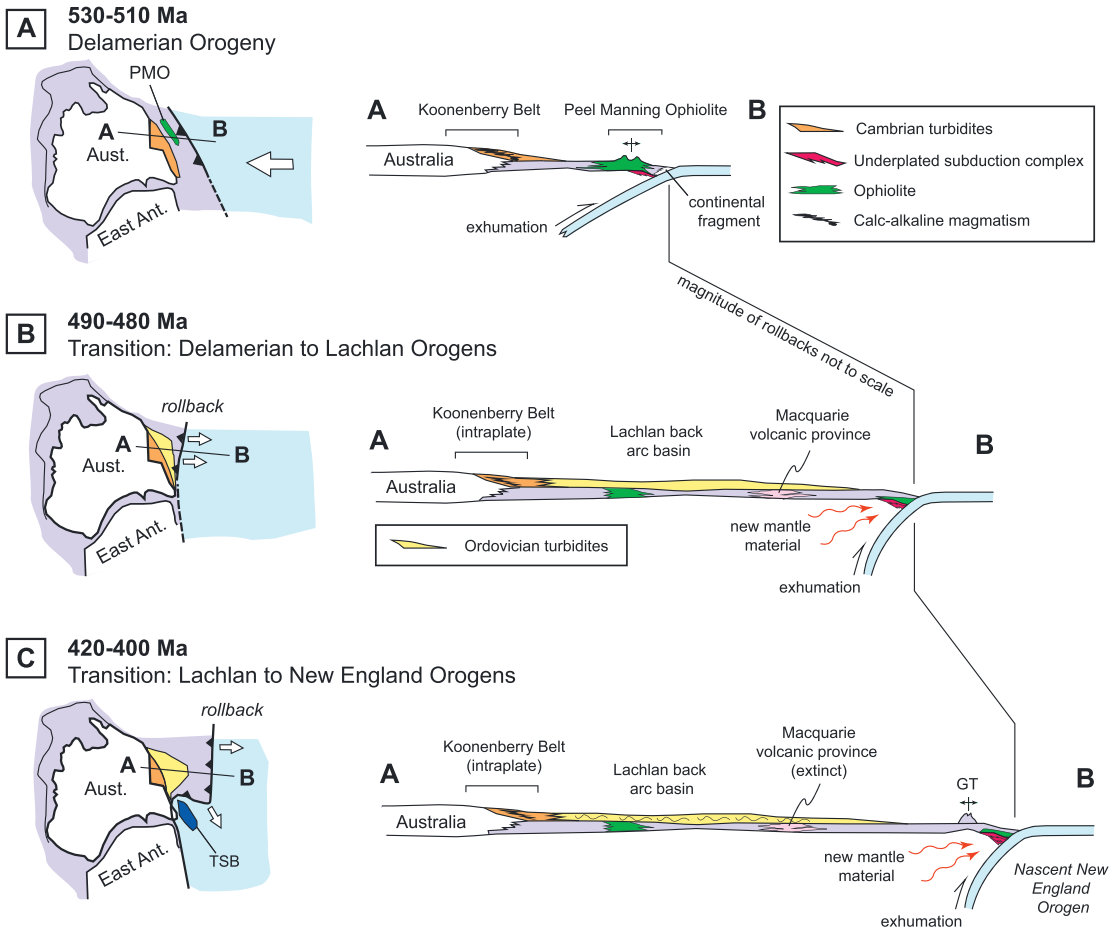

Figure 12. Simplified conceptual model showing a mechanism for how the Peel-Manning Ophiolite and high-pressure rocks were continually translated into the fore-arc of the next orogenic stage. (a) Delamerian Orogeny marks the inception of the Tasmanides. The Peel-Manning Ophiolite (PMO) forms in a suprasubduction setting above a west dipping subduction zone. Exhumation of high-pressure rocks by forced flow resulted in the development of a subduction complex below the ophiolite. Abbreviations: Aust. = Australia; East Ant. = East Antarctica. (b) Rollback responsible for the transition from the Delamerian to the Lachlan orogenies. East directed retreat rifted and detached components of the leading edge of the overriding plate for translation into an outboard position. Consequently, ophiolitic and high-pressure rocks are translated to the east and relocated into a fore-arc position of the new orogenic stage. For simplicity, only the main west dipping subduction zone is shown. We do not preclude the potential for other subduction zones operating in the back-arc region of the Lachlan Orogen such as that currently operating in the Philippine Sea. (c) Second phase of rollback marking the transition from the Lachlan to the New England orogenies. Refer to text for discussion regarding subduction polarity during the formation of the Gamilaroi Terrane. Abbreviations: TSB = Tyennan-Selwyn Block; GT = Gamilaroi Terrane.

plate. In regions were the distance between the trench and continental margin was limited, upper plate convergence potentially resulted in arc-continent collision [*Crawford et al.*, 1984].

As previously discussed, east directed retreat of the subduction zone is a potential mechanism that can account for the transition from the Delamerian to Lachlan orogenic stages [*Foden et al.*, 2006]. It has been recently hypothesized that subduction zone rollback can result in the rifting and translation of rocks from the leading edge of the overriding plate [*Buys et al.*, 2014]. This concept is based on the identification of inherited zircon grains comprising Australian age populations in island arc magmas from the New Hebrides Ridge. These authors suggest that the zircon grains were derived from a continental ribbon, which became detached from the Australian mainland by back-arc extension related to the retreating southwestern Pacific subduction zone [*Schellart et al.*, 2006]. This model provides an elegant mechanism for how rocks formed during an earlier orogenic stage can be translated to the next younger stage during long-lived subduction. Based on this mechanism, the amount of translation would be dependent on the magnitude of retreat and the detached rocks could remain in the fore-arc position of the subduction system. With respect to the evolution of the Tasmanides, it is possible that the retreat of the subduction zone detached parts of the

Peel-Manning Ophiolite and underlying subduction complex from the overriding plate and translated them a considerable distance to the east. Therefore, in addition to the previously discussed metamorphic consequences of rollback, the eastward retreat of the subduction zone can account for the translation of parts of the ophiolite and underlying subduction complex from the Delamerian Orogen to a fore-arc position in the Lachlan Orogen (Figures 12a and 12b).

If rollback is not invoked as the mechanism responsible for the transition from the Delamerian to Lachlan orogenic stages, the alternative model for the Early Ordovician history of the Tasmanides involves two subduction zones, namely, (i) an east dipping subduction zone that was below a magmatic arc (i.e., represented by the Macquarie Volcanic Province) and (ii) a west dipping intraoceanic subduction zone that was located further to the east [*Aitchison and Buckman*, 2012]. In this model, collision and arc accretion along the east dipping subduction zone resulted in lockup and a transference of subduction to the preexisting west dipping subduction zone. Based on this model, the Peel-Manning Ophiolite and high-pressure rocks could form in one of two locations, either within the east dipping or west dipping subduction zones. It is unlikely that the ophiolite and subduction complex formed in the east dipping subduction zone, because collision and accretion would have resulted in the obduction of the ophiolite to the west of the arc (i.e., the Macquarie Volcanic Province). Given that the Peel-Manning Ophiolite is located to the east of the Macquarie Volcanic Province, this cannot be the case. The two-subduction-zone model, therefore, requires the Peel-Manning Ophiolite and high-pressure rocks to have formed in the west dipping intraoceanic subduction zone, which was located in an outboard and isolated position to the main Tasmanides subduction system until the early Devonian. Although this scenario is permissible by our data, we feel that it fails to account for the uncanny overlap between the *P-T-t* histories of high-pressure rocks now located in the New England Orogen and major evolutionary stages of the Delamerian and Lachlan orogenies. Accordingly, we favor a model where the Peel-Manning Ophiolite and associated high-pressure metamorphic rocks formed in the same subduction system responsible for the Delamerian, Lachlan, and New England orogenic stages.

A relatively stable convergent margin setting characterized the evolution of the Lachlan Orogen until the Early Silurian [*Cayley et al*., 2012; *Moresi et al*., 2014]. At this time, a second phase of rollback is interpreted to have resulted in the development of a complex and contorted subduction zone; which was due to the presence of the Tyennan-Selwyn continental block (Figure 12c). In the north, however, rollback was more symmetrical and resulted in the inception of the New England Orogen [*Phillips and Offler*, 2011]. As with the transition from Delamerian to Lachlan orogens, we suggest that the retreat of the subduction zone was responsible for the translation of the Peel-Manning Ophiolite and underlying subduction complex to the New England Orogen (Figure 12c). However, unlike the first rollback stage, where evidence for a spike in geothermal gradient is recorded by the *P-T-t* histories of the high-pressure rocks, a comparable increase in mantle temperatures is not apparent during the Silurian. This can be explained by the continuous exhumation and underplating of high-pressure rocks during the Ordovician-Silurian history of the subduction zone, which would effectively shield the high-pressure rocks located just below the ophiolite from any temperature fluctuations in the mantle wedge.

Our understanding of the Devonian history of the New England Orogen is largely based on studies of the Gamilaroi Terrane, which have led to models involving arc collision and subduction flip [*Aitchison et al*., 1994] or the presence of east and west dipping subduction zones [*Offler and Murray*, 2011]. We suggest that the formation of the Gamilaroi Terrane can be accounted for by a suprasubduction setting, where the terrane formed in the extending fore-arc region of the main west dipping subduction system (Figure 12c). The alternative model, which is also permissible in our reconstruction, is that the Gamilaroi Terrane formed above an east dipping subduction zone [*Aitchison et al*., 1994]. If this was the case, we envisage the east dipping subduction zone to form part of a complex back-arc subduction system that developed behind the main west dipping subduction zone (i.e., Philippine Sea-type setting). Subsequent collision and accretion of the Gamilaroi Terrane in the Late Devonian terminated this subduction zone and resulted in the reconfiguration of the New England Orogen into an east facing Andean-type setting for the Carboniferous.

Final exhumation and exposure of the ophiolite took place along the Peel-Manning Fault System during the Carboniferous-Permian (Figures 13a–13c). It is important to note the structural setting of the high-pressure metamorphic rocks, in that they are located as exotic blocks in the tectonized harzburgite layer of the ophiolite (albeit highly dismembered and serpentinized) as opposed to coherent slabs in a

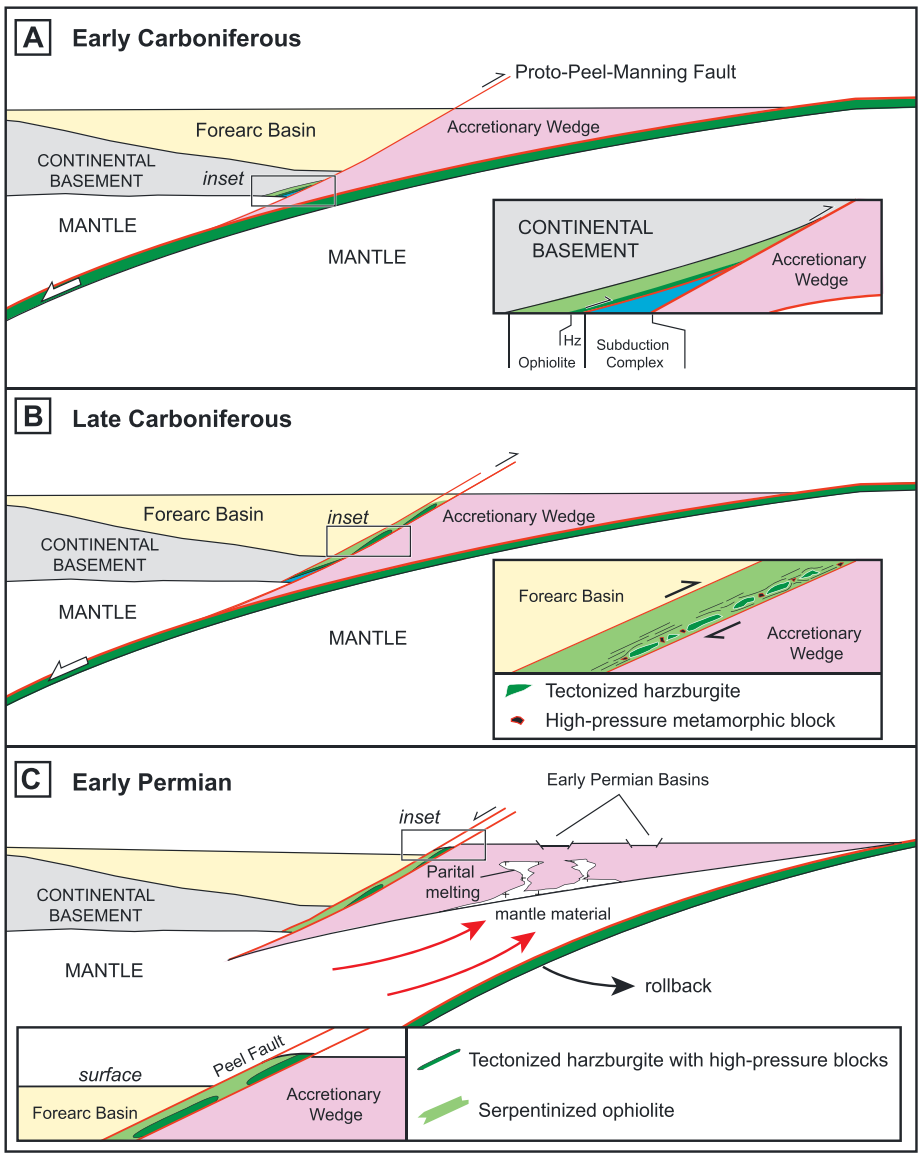

Figure 13. Simplified conceptual model illustrating the emplacement of the Peel-Manning Ophiolite in the southern New England Orogen. (a) Convergence along a west dipping subduction zone during the Carboniferous. Components of earlier subduction stages are present as underplated ophiolitic and high-pressure rocks. Abbreviations: Hz = harzburgite. (b) Thrusting associated with active margin convergence results in shearing of high-pressure rocks from the underlying subduction complex for intercalation within the basal shear zone of the ophiolite. Incipient exhumation of the ophiolite through the crust probably took place during convergence. (c) Extension of the overriding plate during the early Permian results in exposure of the attenuated, heavily serpentinized ophiolite. The high-pressure rocks are located as exotic blocks in the basal, tectonized harzburgite layer of the ophiolite.

subduction complex (cf. Franciscan) [*Wakabayashi*, 2015]. We suggest that the incorporation of high-pressure metamorphic rocks into the basal part of the ophiolite took place by shearing along the underlying subduction complex (Figures 13a and 13b). Blocks of high-pressure metamorphic rocks that were exhumed and underplated during the Cambrian-Devonian history of the subduction zone were therefore plucked from the subduction complex and incorporated within the basal shear zone of the overlying ophiolite. An important implication of this model is that it accounts for the relative scarcity of high-pressure rocks in the New England Orogen when compared with other long-lived accretionary orogens [*Wakabayashi*, 2015].

Thrusting related to convergence probably facilitated the initial transport of the ophiolite along the Peel-Manning Fault System during the Carboniferous (Figure 13b). The identification of serpentinite detritus in the basal sequences of the early Permian Barnard Basin signifies that the exposure of the ophiolite must have taken place by this time (Figure 13c) [*Allan and Leitch*, 1990]. The formation of high-temperature/low-pressure metamorphic complexes [*Dirks et al*., 1992; *Craven et al*., 2012], emplacement of the S-type plutonic rocks of the New England Batholith (Figure 13c) [*O'Neil et al*., 1977; *Shaw and Flood*, 1981; *Hensel et al*., 1985; *Cawood et al*., 2011; *Rosenbaum et al*., 2012], and development of the Barnard Basin [*Leitch*, 1988] all coincided with this time period. Extension in the overriding plate is suggested as the primary mechanism responsible for the development of these geological features [*Jenkins et al*., 2002; *Phillips et al*., 2008; *Rosenbaum et al*., 2012], which may have been caused by east directed rollback (Figure 13c) [*Jenkins et al*., 2002] or a change from a convergent to transform setting [*Aitchison and Flood*, 1992]. Irrespective of the geodynamic setting, the aforementioned temporal correlation supports a relationship between extension and transtension of the overriding plate resulting in the final exposure of the ophiolite by normal faulting in the early-middle Permian (Figure 13c).

7. Summary

Pressure-temperature-time histories of high-pressure metamorphic rocks in the Peel-Manning Ophiolite correlate in time with a major geodynamic event in the Tasmanides. Our new U-Pb zircon age revises the timing of eclogite facies metamorphism to 514 ± 6 Ma, which overlaps with the early stages of the Delamerian Orogeny. We therefore suggest that the multiple-subduction zone model for the early Cambrian evolution of the Tasmanides [*Glen*, 2013] is not required. Exhumation and recrystallization of high-pressure rocks at amphibolite-blueschist facies conditions took place between 490 and 480 Ma, which coincides with the transition from the Delamerian and Lachlan orogenies. This transition was probably driven by rollback of the subduction zone, which resulted in the injection of new material into the mantle wedge and heating of the subduction zone. The associated temperature increase is recorded in all high-pressure samples by the growth of amphibolite facies mineral assemblages. Following this, recrystallization of selective samples at blueschist facies conditions is consistent with exhumation and metamorphism in a stable and cooling subduction zone.

In addition to the thermal response, rollback also detached parts of the Peel-Manning Ophiolite and high-pressure rocks of the underlying subduction complex from the fore-arc region of the Delamerian Orogen, translating them outboard to the Lachlan Orogen. A second phase of east directed rollback in the Late Silurian again translated the ophiolite and subduction complex to the New England Orogen where it was subsequently exhumed through the crust along the Peel-Manning Fault System. Exposure of the ophiolite was probably related to a combination of early thrusting driven by active margin convergence, followed by extension of the upper plate. Shearing of the ophiolite over the underlying subduction complex during exhumation through the crust incorporated blocks of high-pressure metamorphic rocks into the basal, tectonized harzburgite layer of the ophiolite. This is why high-pressure rocks in the Tasmanides are only exposed as rare exotic blocks rather than large coherent tracts of a subduction complex.

Given the temporal overlap between the *P-T-t* histories recorded by high-pressure metamorphic rocks and major geodynamic events in the Tasmanides, we support a link between the evolution of these rocks and a long-lived west dipping eastward retreating subduction zone. This study also highlights a potential link between subduction rollback and far-traveled outboard translation of fore-arc components.

Acknowledgments
We thank Jeffrey Huang for discussions related to the interpretation of U-Pb data. Joel Fitzherbert is acknowledged for discussions on the evolution of high-pressure metamorphic rocks. Isotope analyses were financially assisted by a University of Newcastle Research grant awarded to G.P. Analyses were carried out in the Electron Microscope and X-ray Unit at The University of Newcastle. The data for this paper are available by contacting the corresponding author. G. Phillips publishes with permission of the Director of the Geological Survey of New South Wales.

References

Aitchison, J. C., and S. Buckman (2012), Accordion vs. quantum tectonics: Insights into continental growth processes from the Paleozoic of eastern Gondwana, *Gondwana Res.*, *22*, 674–680.

Aitchison, J. C., and P. G. Flood (1992), Early Permian transform margin development of the southern New England Orogen, eastern Australia (eastern Gondwana), *Tectonics*, *11*, 1385–1391, doi:10.1029/92TC01003.

Aitchison, J. C., and P. G. Flood (1994), Gamilaroi Terrane: A Devonian rifted intra-oceanic island-arc assemblage, NSW, Australia, in *Volcanism Associated With Extension at Consuming Plate Margins*, edited by J. L. Smellie, *Geol. Soc. London Spec. Publ.*, *81*, 155–168.

Aitchison, J. C., and T. R. Ireland (1995), Age profile of ophiolitic rocks across the Late Palaeozoic New England Orogen, New South Wales: Implications for tectonic models, *Aust. J. Earth Sci.*, *42*, 11–23.

Aitchison, J. C., M. C. Blake, P. G. Flood, and B. L. Murchey (1988), New and revised lithostratigraphic units from the southwestern New England Fold Belt, Geol. Surv. of New South Wales, *Q. Notes*, *72*, 10–16.

Aitchison, J. C., T. R. Ireland, M. C. Blake, and P. G. Flood (1992), 530 Ma zircon age for ophiolite from the New England Orogen: Oldest rocks known from eastern Australia, *Geology*, *20*, 125–128.

Aitchison, J. C., M. C. Blake, P. G. Flood, and A. S. Jayko (1994), Paleozoic ophiolitic assemblages within the southern New England orogen of eastern Australia: Implications for growth of the Gondwana margin, *Tectonics*, *13*, 1135–1149, doi:10.1029/93TC03550.
Allan, A. D., and E. C. Leitch (1990), The tectonic significance of uncomformable contacts at the base of Early Permian sequences, southern New England Fold Belt, *Aust. J. Earth Sci.*, *37*, 43–49.
Arnaud, N. O., and S. P. Kelley (1995), Evidence for excess argon during high pressure metamorphism in the Dora Maira massif (Western Alps, Italy), using an ultra-violet laser ablation microprobe ^{40}Ar-^{39}Ar technique, *Contrib. Mineral. Petrol.*, *121*, 1–11.
Black, L. P., S. L. Kamo, C. M. Allen, J. M. Aleinikoff, D. W. Davis, R. J. Korsch, and C. Foudoulis (2003), TEMORA 1: A new zircon standard for Phanerozoic U-Pb geochronology, *Chem. Geol.*, *200*, 155–170.
Blake, M. C., and B. L. Murchey (1988), A Californian model for the New England Fold Belt, *Geol. Surv. N. S. W. Q. Notes*, *72*, 1–16.
Brown, E. H. (1977), The crosstie content of Ca-amphibole as a guide to pressure of metamorphism, *J. Petrol.*, *18*, 53–72.
Buys, J., C. Spandler, R. J. Holm, and S. W. Richards (2014), Remnants of ancient Australia in Vanuatu: Implications for crustal evolution in island arcs and tectonic development of the southwest Pacific, *Geology*, *42*, 939–942.
Cawood, P. A. (1983), Modal composition and detrital clinopyroxene geochemistry of lithic sandstone from the New England Fold Belt (east Australia): A Paleozoic forearc terrane, *Geol. Soc. Am. Bull.*, *94*, 1194–1214.
Cawood, P. A. (2005), Terra Australis Orogen: Breakup and development of the Pacific and Iapetus margins of Gondwana during the Neoproterozoic and Paleozoic, *Earth Sci. Rev.*, *69*, 249–279.
Cawood, P. A., S. A. Pisarevsky, and E. C. Leitch (2011), Unraveling the New England Orocline, east Gondwana accretionary margin, *Tectonics*, *30*, TC5002, doi:10.1029/2011TC002864.
Cayley, R. A. (2011), Exotic crustal block accretion to the eastern Gondwanaland margin in the Late Cambrian-Tasmania, the Selwyn Block, and implications for the Cambrian-Silurian evolution of the Ross, Delamerian, and Lachlan Orogens, *Gondwana Res.*, *19*, 628–649.
Cayley, R. A., R. Musgrave, and W. Preiss (2012), South-directed oroclinal folding in the Lachlan Fold Belt: A solution to apparent Ordovician-Early Silurian complexity. Program and Abstracts, SGTSG biennial conference, Waratah Bay, Australia, *Geol. Soc. Aust. Abstr.*, *102*, 19–21.
Cherniak, D. J., and E. B. Watson (2001), Pb diffusion in zircon, *Chem. Geol.*, *172*, 5–24.
Cherniak, D. J., J. M. Hanchar, and E. B. Watson (1997), Rare-earth diffusion in zircon, *Chem. Geol.*, *134*, 289–301.
Cloos, M. (1982), Flow melanges: Numerical modeling and geologic constraints on their origin in the Franciscan subduction complex, California, *Geol. Soc. Am. Bull.*, *93*, 330–345.
Coleman, R. G., D. E. Lee, L. B. Beatty, and W. W. Brannock (1965), Eclogite and eclogite: Their differences and similarities, *Geol. Soc. Am. Bull.*, *76*, 483–508.
Collins, W. J. (2002), Hot orogens, tectonic switching, and creation of continental crust, *Geology*, *30*, 535–538.
Colquhoun, G. P., G. Phillips, K. S. Hughes, L. Deyssing, J. A. Fitzherbert, and A. L. Troedson (2015), New South Wales zone 56 seamless geology version 1 [digital dataset], Geol. Surv. of New South Wales, Maitland.
Craven, S. J., N. R. Daczko, and J. A. Halpin (2012), Thermal gradient and timing of high-*T*-low-*P* metamorphism in the Wongwibinda Metamorphic Complex, southern New England Orogen, Australia, *J. Metamorph. Geol.*, *30*, 3–20.
Crawford, A. J., and R. F. Berry (1992), Tectonic implications of Late Proterozoic-Early Palaeozoic igneous rock associations in western Tasmania, *Tectonophysics*, *30*, 37–56.
Crawford, A. J., W. E. Cameron, and R. R. Keays (1984), The association boninite low-Ti andesite-tholeiite in the Heathcote greenstone belt, Victoria; ensimatic setting for the early Lachlan fold belt, *Aust. J. Earth Sci.*, *31*, 161–175.
Crawford, A. J., B. P. J. Stevens, and M. Fanning (1997), Geochemistry and tectonic setting of some Neoproterozoic and Early Cambrian volcanics in western New South Wales, *Aust. J. Earth Sci.*, *44*, 831–852.
Crawford, A. J., S. Meffre, R. J. Squire, L. M. Barron, and T. J. Falloon (2007), Middle and Late Ordovician magmatic evolution of the Macquarie Arc, Lachlan Orogen, New South Wales, *Aust. J. Earth Sci.*, *54*, 181–214.
Cross, K. (1983), The Pigna Barney Ophiolitic Complex and associated basaltic rocks, Northeastern New South Wales, Australia PhD thesis, p. 283, Univ. of New England, Armidale, N. S. W.
Dirks, P. H. G. M., M. Hand, W. J. Collins, and R. Offler (1992), Structural-metamorphic evolution of the Tia Complex, New England Fold Belt; thermal overprint of an accretion-subduction complex in a compressional back-arc setting, *J. Struct. Geol.*, *14*, 669–688.
Ernst, W. G., and J. Liu (1998), Experimental phase-equilibrium study of Al- and Ti-contents of calcic amphibole in MORB-A semiquantitative thermobarometer, *Am. Mineral.*, *83*, 952–969.
Essene, E. J., and W. S. Fyfe (1967), Omphacite in California metamorphic rocks, *Contrib. Mineral. Petrol.*, *15*, 1–23.
Fanning, C. M., E. C. Leitch, and T. Watanabe (2002), An updated assessment of the SHRIMP U-Pb Zircon dating of the Attunga eclogite in New South Wales, Australia: Relevance to the Pacific Margin of Gondwana International Symposium on the Amalgamation of Precambrian Blocks and the Role of the Paleozoic Orogens in Asia, Sapporo, Japan.
Fergusson, C. L. (2003), Ordovician-Silurian accretion tectonics of the Lachlan Fold Belt, southeastern Australia, *Aust. J. Earth Sci.*, *50*, 475–490.
Fergusson, C. L. (2014), Late Ordovician to mid-Silurian Benambran subduction zones in the Lachlan Orogen, southeastern Australia, *Aust. J. Earth Sci.*, *61*, 587–606.
Fergusson, C. L., and P. J. Coney (1992), Convergence and intraplate deformation in the Lachlan Fold Belt of Southeastern Australia, *Tectonophysics*, *214*, 433–439.
Ferry, J. M., and E. B. Watson (2007), New thermodynamic models and revised calibrations for the Ti-in-zircon and Zr-in-rutile thermometers, *Contrib. Mineral. Petrol.*, *154*, 429–437.
Fleck, R. J., J. F. Sutter, and D. H. Elliot (1977), Interpretation of discordant ^{40}Ar/^{39}Ar age-spectra of Mesozoic tholeiites from Antarctica, *Geochim. Cosmochim. Acta*, *41*, 15–32.
Foden, J., M. A. Elburg, J. Dougherty-Page, and A. Burtt (2006), The timing and duration of the Delamerian Orogeny: Correlation with the Ross Orogen and implications for Gondwana assembly, *J. Geol.*, *114*, 189–210.
Foster, D. A., and D. R. Gray (2000), Evolution and structure of the Lachlan Fold Belt (Orogen) of Eastern Australia, *Annu. Rev. Earth Planet. Sci.*, *28*, 47–80.
Frey, M., C. De Capitani, and J. G. Liou (1991), A new petrogenetic grid for low-grade metabasites, *J. Metamorph. Geol.*, *9*, 497–509.
Fukui, S., T. Watanabe, T. Itaya, and E. C. Leitch (1995), Middle Ordovician high PT metamorphic rocks in eastern Australia: Evidence from K-Ar ages, *Tectonics*, *14*, 1014–1020, doi:10.1029/94TC01317.
Fukui, S., T. Tsujimori, T. Watanabe, and T. Itaya (2012), Tectono-metamorphic evolution of high-P/T and low-P/T metamorphic rocks in the Tia Complex, southern New England Fold Belt, eastern Australia: Insights from K-Ar chronology, *J. Asian Earth Sci.*, *59*, 62–69.
Gerya, T., B. Stockhert, and A. Perchuk (2002), Exhumation of high-pressure metamorphic rocks in a subduction channel: A numerical simulation, *Tectonics*, *21*(6), 1056, doi:10.1029/2002TC001406.
Glen, R. A. (2005), The Tasmanides of eastern Australia, in *Terrane Processes at the Margins of Gondwana*, *Geol. Soc. London Spec. Publ.*, *246*, 23–96.

Glen, R. A. (2013), Refining accretionary orogen models for the Tasmanides of eastern Australia, *Aust. J. Earth Sci.*, *60*, 315–370.
Glen, R. A., J. L. Walshe, L. M. Barron, and J. J. Watkins (1998), Ordovician convergent-margin volcanism & tectonism in the Lachlan sector of east Gondwana, *Geology*, *26*, 751–754.
Gray, D. R., and D. A. Foster (1997), Orogenic concepts—Application and definition: Lachlan fold belt, eastern Australia, *Am. J. Sci.*, *297*, 859–891.
Gray, D. R., and D. A. Foster (2004), Tectonic evolution of the Lachlan Orogen, southeast Australia: Historical review, data synthesis and modern perspectives, *Aust. J. Earth Sci.*, *51*, 773–817.
Greenfield, J. E., R. J. Musgrave, M. C. Bruce, P. J. Gilmore, and K. J. Mills (2011), The Mount Wright Arc: A Cambrian subduction system developed on the continental margin of East Gondwana, Koonenberry Belt, eastern Australia, *Gondwana Res.*, *19*, 650–669.
Hames, W. E., and S. A. Bowring (1994), An empirical evaluation of the argon diffusion geometry in muscovite, *Earth Planet. Sci. Lett.*, *124*, 161–167.
Hensel, H. D., M. T. McCulloch, and B. W. Chappell (1985), The New England Batholith: Constraints on its derivation from Nd and Sr isotopic studies of granitoids and country rocks, *Geochim. Cosmochim. Acta*, *49*, 369–384.
Hermann, J., and D. Rubatto (2003), Relating zircon and monazite domains to garnet growth zones: Age and duration of granulite facies metamorphism in the Val Malenco lower crust, *J. Metamorph. Geol.*, *21*, 833–852.
Holland, T. (1980), The reaction albite = jadeite + quartz determined experimentally in the range 600–1200°C, *Am. Mineral.*, *65*, 129–134.
Ishiga, H., E. C. Leitch, T. Watanabe, T. Naka, and M. Iwasaki (1988), Radiolarian and conodont biostratigraphy of siliceous rocks from the New England Fold Belt, *Aust. J. Earth Sci.*, *35*, 73–80.
Jenkins, R. B., B. Landenberger, and W. J. Collins (2002), Late Palaeozoic retreating and advancing subduction boundary in the New England Fold Belt, New South Wales, *Aust. J. Earth Sci.*, *49*, 467–489.
Kelley, S. (2002), Excess argon in K-Ar and Ar-Ar geochronology, *Chem. Geol.*, *188*, 1–22.
Kemp, A. I. S., C. J. Hawkesworth, W. J. Collins, C. M. Gray, P. L. Blevin, and EIMF (2009), Isotopic evidence for rapid continental growth in an extensional accretionary orogen: The Tasmanides, eastern Australia, *Earth and Planet. Sci.*, *284*, 455–466.
Kincaid, C., and R. W. Griffiths (2003), Laboratory models of the thermal evolution of the mantle during rollback subduction, *Nature*, *425*, 58–62.
Korsch, R. J., D. W. Johnstone, and K. D. Wake-Dyster (1997), Crustal architecture of the New England Orogen based on deep seismic reflection profiling, in *Tectonics and Metallogenesis of the New England Orogen*, edited by P. M. Ashley and P. G. Flood, *Geol. Soc. Australia Spec. Publ.*, *19*, 29–51.
Krogh-Ravna, E. (2000), The garnet-clinopyroxene Fe^{2+}-Mg geothermometer: An updated calibration, *J. Metamorph. Geol.*, *18*, 211–219.
Leake, B. E., et al. (1997), Nomenclature of amphiboles: Report of the Subcommittee on Amphiboles of the International Mineralogical Association, Commission on New Minerals and Mineral Names, *Can. Mineral.*, *35*, 219–246.
Leitch, E. C. (1974), The geological development of the southern part of the New England Fold Belt, *Aust. J. Earth Sci.*, *21*, 133–156.
Leitch, E. C. (1988), The Barnard Basin and the early Permian development of the southern part of the New England Fold Belt, in *New England Orogen Tectonics and Metallogenesis*, edited by J. D. Kleeman, pp. 61–67, Dep. of Geol. and Geophys., Univ. of New England, Armidale, N. S. W.
Leitch, E. C., and P. A. Cawood (1987), Provenance determination of volcaniclastic rocks: The nature and tectonic significance of Cambrian conglomerate from the New England Fold Belt, eastern Australia, *J. Sediment. Petrol.*, *57*, 630–638.
Ludwig, K. R. (2003), Isoplot/Ex version 3.0, in *A Geochronological Toolkit for Microsoft Excel*, *Berkeley Geochronol. Cent. Spec. Publ.*, vol. 4, 70 pp., Berkeley.
Maruyama, S., M. Cho, and J. G. Liou (1986), Experimental investigations of blueschist-greenschist transition equilibria: Pressure dependence of Al_2O_3 contents in sodic amphiboles—A new geobarometer, in *Blueschist and Eclogites*, edited by B. W. Evans and E. H. Brown, *Mem. Geol. Soc. Am.*, *164*, 1–16.
McDonough, W. F., and S. Sun (1995), The composition of the Earth, *Chem. Geol.*, *120*(3–4), 223–253.
McPhie, J. (1984), Permo-Carboniferous silicic volcanism and palaeogeography on the western edge of the New England Orogen, north-eastern New South Wales, *Aust. J. Earth Sci.*, *31*, 133–146.
McPhie, J. (1987), Andean analogues for the Late Carboniferous volcanic arc and arc flank environment of the western New England Orogen, New South Wales, Australia, *Tectonophysics*, *138*, 269–288.
Meffre, S., R. J. Scott, R. A. Glen, and R. J. Squire (2007), Re-evaluation of contact relationships between Ordovician volcanic belts and the quartz-rich turbidites of the Lachlan Orogen, *Aust. J. Earth Sci.*, *54*, 363–383.
Moresi, L., P. G. Betts, M. S. Miller, and R. A. Cayley (2014), Dynamics of continental accretion, *Nature*, *508*, 245–248.
O'Hanley, D. S., and R. Offler (1992), Characterization of multiple serpentinization, Woodsreef, New South Wales, *Can. Mineral.*, *30*, 1113–1126.
O'Neil, J. R., S. E. Shaw, and R. H. Flood (1977), Oxygen and hydrogen isotope compositions as indicators of granite genesis in the New England Batholith, Australia, *Contrib. Mineral. Petrol.*, *62*, 313–328.
Offler, R. (1982), The origin of exotic blocks in serpentinites, Peel Fault System, Glenrock Station, N.S.W, in *New England Geology*, edited by P. G. Flood and B. Runnegar, pp. 43–52, Dep. of Geol., Univ. of New England, Armidale, N. S. W.
Offler, R. (1999), Origin and significance of blueschist "knockers", Glenrock Station, NSW, in *New England Orogen; Regional Geology, Tectonics and Metallogenesis*, edited by P. G. Flood, pp. 35–44, Dep. of Geol. and Geophys., Univ. of New England, Armidale, N. S. W.
Offler, R., and C. Murray (2011), Devonian volcanics in the New England Orogen: Tectonic setting and polarity, *Gondwana Res.*, *19*, 706–715.
Offler, R., and J. Gamble (2002), Evolution of an intra-oceanic island arc during the Late Silurian-Late Devonian, New England Fold Belt, Australia, *Aust. J. Earth Sci.*, *49*, 349–366.
Offler, R., and S. Shaw (2006), Hornblende Gabbro Block in serpentinite mélange, Peel-Manning Fault System, New South Wales, Australia: Lu-Hf and U-Pb isotopic evidence for mantle derived, Late Ordovician igneous activity, *J. Geol.*, *114*, 211–230.
Peacock, S. M. (1996), Thermal and petrological structure of subduction zones, in *Subduction Top to Bottom*, *Geophys. Monogr.*, vol. 96, edited by G. E. Bebout et al., pp. 119–133, AGU, Washington, D. C.
Pearce, J. A. (1983), Role of sub-continental lithosphere in magma genesis at active continental margins, in *Continental Basalts and Mantle Xenoliths*, edited by C. J. Hawkesworth and M. J. Norry, pp. 230–249, Shiva, Nantwich.
Pearce, J. A. (2014), Immobile element fingerprinting of ophiolites, *Elements*, *10*, 101–108.
Pearce, N. J. G., W. T. Perkins, J. A. Westgate, M. P. Gorton, S. E. Jackson, C. R. Neal, and S. P. Chenery (1997), A compilation of new and published major and trace element data for NIST SRM 610 and NIST SRM 612 glass reference materials, *Geostand. Newsl.*, *21*, 115–144.
Phillips, D., and J. W. Harris (2008), Provenance studies from $^{40}Ar/^{39}Ar$ dating of mineral inclusions in diamonds: Methodological tests on the Orapa kimberlite, Botswana, *Earth Planet. Sci. Lett.*, *274*, 169–178.

Phillips, G., and R. Offler (2011), Contrasting modes of eclogite and blueschist exhumation in a retreating subduction system: The Tasmanides, Australia, *Gondwana Res.*, *19*, 800–811.
Phillips, G., C. J. L. Wilson, D. Phillips, and S. K. Szczepanski (2007), Thermochronological ($^{40}Ar/^{39}Ar$) evidence of Early Palaeozoic basin inversion within the southern Prince Charles Mountains, East Antarctica: Implications for East Gondwana, *J. Geol. Soc. London*, *164*, 771–784.
Phillips, G., R. Offler, and M. Hand (2008), *P-T-t* deformation framework of an accretionary prism, southern New England Orogen, eastern Australia: Implications for blueschist exhumation and metamorphic switching, *Tectonics*, *27*, TC6017, doi:10.1029/2008TC002323.
Phillips, G., B. Landenberger, and E. A. Belousova (2011), Building the New England Batholith, eastern Australia—Linking granite petrogenesis with geodynamic setting using Hf isotopes in zircon, *Lithos*, *122*, 1–12.
Powell, C. M. A. (1983), Tectonic relationship between the late Ordovician and Late Silurian palaeogeographies of southeastern Australia, *J. Geol. Soc. Aust.*, *30*, 353–373.
Powell, R., and T. J. B. Holland (1994), Optimal geothermometry and geobarometry, *Am. Mineral.*, *79*, 120–133.
Quinn, C. D., I. G. Percival, R. A. Glen, and W. J. Xiao (2014), Ordovician marginal basin evolution near the palaeo-Pacific east Gondwana margin, Australia, *J. Geol. Soc. London*, *171*, 723–736.
Roberts, J., W. Wang, and M. C. Fanning (2003), Stratigraphy and correlation of Carboniferous ignimbrites, Rocky Creek region, Tamworth Belt, Southern New England Orogen, New South Wales, *Aust. J. Earth Sci.*, *50*, 931–954.
Roberts, J., R. Offler, and M. C. Fanning (2004), Upper Carboniferous to Lower Permian volcanic successions of the Carroll-Nandewar region, northern Tamworth Belt, southern New England Orogen, Australia, *Aust. J. Earth Sci.*, *51*, 205–232.
Roberts, J., R. Offler, and M. C. Fanning (2006), Carboniferous to Lower Permian stratigraphy of the southern Tamworth Belt, southern New England Orogen, Australia: Boundary sequences of the Werrie and Rouchel blocks, *Aust. J. Earth Sci.*, *53*, 249–284.
Rosenbaum, G., P. Li, and D. Rubatto (2012), The contorted New England Orogen (eastern Australia): New evidence from U-Pb geochronology of early Permian granitoids, *Tectonics*, *31*, TC1006, doi:10.1029/2011TC002960.
Rubatto, D. (2002), Zircon trace element geochemistry: Distribution coefficients and the link between U-Pb ages and metamorphism, *Chem. Geol.*, *184*, 123–138.
Rubatto, D., D. Gebauer, and M. C. Fanning (1998), Jurassic formation and Eocene subduction of the Zermatt-Saas-Fee ophiolites: Implications for the geodynamic evolution of the Central and Western Alps, *Contrib. Mineral. Petrol.*, *132*, 269–287.
Sano, S., R. Offler, H. Hyodo, and T. Watanabe (2004), Geochemistry and chronology of tectonic blocks in serpentinite mélange of the Southern New England Fold Belt, NSW, Australia, *Gondwana Res.*, *7*, 817–831.
Schellart, W. P., G. S. Lister, and V. G. Toy (2006), A Late Cretaceous and Cenozoic reconstruction of the Southwest Pacific region: Tectonics controlled by subduction and slab rollback processes, *Earth Sci. Rev.*, *76*, 191–233.
Shaw, S. E., and R. H. Flood (1974), Eclogite from serpentinite near Attunga, New South Wales, *Aust. J. Earth Sci.*, *21*, 377–385.
Shaw, S. E., and R. H. Flood (1981), The New England Batholith, eastern Australia: Geochemical variations in time and space, *J. Geophys. Res.*, *86*, 10,530–10,544, doi:10.1029/JB086iB11p10530.
Stacey, J. S., and J. D. Kramers (1975), Approximation of terrestrial lead evolution by a two-stage model, *Earth Planet. Sci. Lett.*, *26*, 207–221.
Stern, R. J. (2004), Subduction initiation: Spontaneous and induced, *Earth Planet. Sci. Lett.*, *226*, 275–292.
Sun, S. S., and W. F. McDonough (1989), Chemical and isotopic characteristics of oceanic basalts. Implications for mantle composition and processes, in *Magmatism in the Ocean Basins*, edited by A. D. Saunders and M. J. Norry, *Geol. Soc. London Spec. Publ.*, *42*, 313–345.
Vandenberg, A. H. M. (1999), Timing of orogenic events in the Lachlan Orogen, *Aust. J. Earth Sci.*, *46*, 691–701.
Wakabayashi, J. (2015), Anatomy of a subduction complex: Architecture of the Franciscan Complex, California, at multiple length and time scales, *Int. Geol. Rev.*, *57*, 669–743, doi:10.1080/00206814.2014.998728.
Wilkinson, J. F. G. (1971), The petrology of some vitrophyric calcalkaline volcanics from the Carboniferous of New South Wales, *J. Petrol.*, *12*, 587–619.
Williams, I. S. (1998), U-Th-Pb geochronology by ion microprobe, *Rev. Econ. Geol.*, *7*(1), 1–35.
Xia, Q. X., Y. F. Zheng, H. Yuan, and F. Y. Wu (2009), Contrasting Lu-Hf and U-Th-Pb isotope systematics between metamorphic growth and recrystallization of zircon from eclogite-facies metagranites in the Dabie orogen, China, *Lithos*, *112*, 477–496.
Yang, K., and P. K. Seccombe (1997), Geochemistry of the mafic and ultramafic complexes of the northern Great Serpentinite Belt, New South Wales: Implications for first-stage melting, in *Tectonics and Metallogenesis of the New England Orogen*, edited by P. M. Ashley and P. G. Flood, *Geol. Soc. Aust. Spec. Publ.*, *19*, 197–211.

Erratum

In the originally published version of this article, the Figure 10 caption was incorrect. The caption has since been corrected, and this version may be considered the authoritative version of record.